Check for updates

Paleoceanography and Paleoclimatology

AGU ADVANCING EARTH AND SPACE SCIENCES

RESEARCH ARTICLE
10.1029/2023PA004772

Rock Magnetic-Based Cyclic Expression in Late Visean Ramp Carbonates and an Astrochronology for the Late Asbian From Northwest England

Mark W. Hounslow[1,2], Pedro Cózar[3], Ian D. Somerville[4], and Andrew J. Biggin[2]

[1]Lancaster Environment Centre, Lancaster University, Lancaster, UK, [2]Earth, Ocean and Ecological Sciences, University of Liverpool, Liverpool, UK, [3]Instituto de Geociencias (CSIC-UCM), Madrid, Spain, [4]UCD School of Earth Sciences, University College Dublin, Belfield, Ireland

Key Points:

- Rock magnetic properties show the included siliciclastics are from hematite-rich eolian dust and marine-dispersed sources
- The magnetite mineral abundance proxies principally carry the primary eccentricity-driven astronomical signal
- An astrochronology for the late Asbian indicates its duration is 1976 ± 86 kyr

Supporting Information:

Supporting Information may be found in the online version of this article.

Correspondence to:

M. W. Hounslow,
m.hounslow@lancaster.ac.uk

Citation:

Hounslow, M. W., Cózar, P., Somerville, I. D., & Biggin, A. J. (2024). Rock magnetic-based cyclic expression in late Visean ramp carbonates and an astrochronology for the late Asbian from northwest England. *Paleoceanography and Paleoclimatology*, *39*, e2023PA004772. https://doi.org/10.1029/2023PA004772

Received 27 SEP 2023
Accepted 23 JAN 2024

Author Contributions:

Conceptualization: Mark W. Hounslow
Data curation: Mark W. Hounslow
Formal analysis: Mark W. Hounslow, Pedro Cózar
Funding acquisition: Mark W. Hounslow, Andrew J. Biggin
Investigation: Mark W. Hounslow
Methodology: Mark W. Hounslow
Project administration: Mark W. Hounslow
Resources: Mark W. Hounslow, Pedro Cózar, Andrew J. Biggin
Software: Mark W. Hounslow
Supervision: Mark W. Hounslow
Validation: Mark W. Hounslow
Visualization: Mark W. Hounslow
Writing – original draft: Mark W. Hounslow, Pedro Cózar, Ian D. Somerville

© 2024. The Authors.
This is an open access article under the terms of the Creative Commons Attribution License, which permits use, distribution and reproduction in any medium, provided the original work is properly cited.

Abstract The late Asbian appears to mark the initial, well-documented, onset of far-field glacio-eustatic changes in equatorial Mississippian strata. This work unravels the nature of cyclicity in upper Asbian shallow marine carbonates, using a combination of petrographic study, rock magnetic proxies and astrochronological testing on samples from the Trowbarrow section, NW England. Rock magnetic data express the content of two types of siliciclastic sources; a marine-delivered magnetite-dominated source, and an eolian-delivered, hematite-dominated source. The eolian-sourced material generally peaked during regressive and low-stand parts of the carbonate rhythms. Astrochronologic testing methods based around the average spectral misfit and TimeOpt methodology show the magnetite abundance proxies are principally carrying the astronomically forced signal. Two likely sedimentation rate models are derived from the five better magnetic proxies using evolutive methods. In addition, a set of three likely major hiatus levels are inferred in the sedimentation rate models, based on testing possible major hiatus scenarios with TimeOpt methods, using eccentricity modulation. From these, using the three best proxies, an average astrochronologic duration for the Trowbarrow section suggests a late Asbian duration of 1976 ± 86 kyr (1σ), and a basal late Asbian age of 334.48 ± 0.35 Ma (2σ). Coupled atmosphere-ocean models for the late Paleozoic, suggest that lows in short eccentricity correspond to glacials, when inferred delivery of siliciclastic sediment to the carbonate ramp is generally at a maximum. The glacial and lower sea-level intervals also coincide with maximum delivery of eolian siliciclastics, likely linked to increased aridity and less vegetation cover on adjacent and distal parts of Laurentia.

Plain Language Summary Around 332–333 million years ago changes in sea-level driven by changes in polar ice volume were an important control on the sedimentation patterns through time in carbonates from low paleolatitudes. Understanding the pacing of these changes has implications for timescales and paleoceanographic processes. These cyclical changes in carbonate lithology are related to changes in magnetic properties within the late Asbian (late Visean) section at Trowbarrow in NW England. The magnetic changes principally express differences in the small content of silica-based clastics, but also reflect changing Fe-oxide mineralogy between times of hematite-rich and magnetite-rich clastic input. The changes are responding to differences in eolian delivery and marine dispersal of the clastics. Eolian delivery of clastics was at its peak near sea-level lowstands, when nearby terrestrial systems were the most arid and supplying the most dust. Statistical assessments show that the magnetite abundance signal principally expresses changes in astronomical eccentricity. Primarily using the expected eccentricity pacing, two age models are constructed, which includes three levels of detectable hiatus in the section. Using these two age models and the three best magnetic proxies, the average late Asbian duration is 1976 ± 86 kyr, with the base of the late Asbian at 334.48 ± 0.35 Ma.

1. Introduction

The Late Paleozoic ice age (LPIA) is the most prolonged ice-house interval in the Phanerozoic. It has many similarities in Earth-System dynamics to the Cenozoic icehouse established in the Oligocene (Montañez, 2022). The deposits produced by the LPIA were largely focussed on the southern Hemisphere during the Carboniferous, but with ice-volume changes also likely reflected in low- and mid-latitude deposits, probably through mechanisms driven by glacio-eustatic sea-level change (Fielding et al., 2008). These principally drove cyclic sedimentation or cyclothems most marked in the Pennsylvanian (Fielding, 2021; Ueno et al., 2013), but similar forcing was present in the Middle and Late Mississippian. Milankovitch-style astronomical forcing seems to have

Writing – review & editing: Mark W. Hounslow, Pedro Cózar, Ian D. Somerville, Andrew J. Biggin

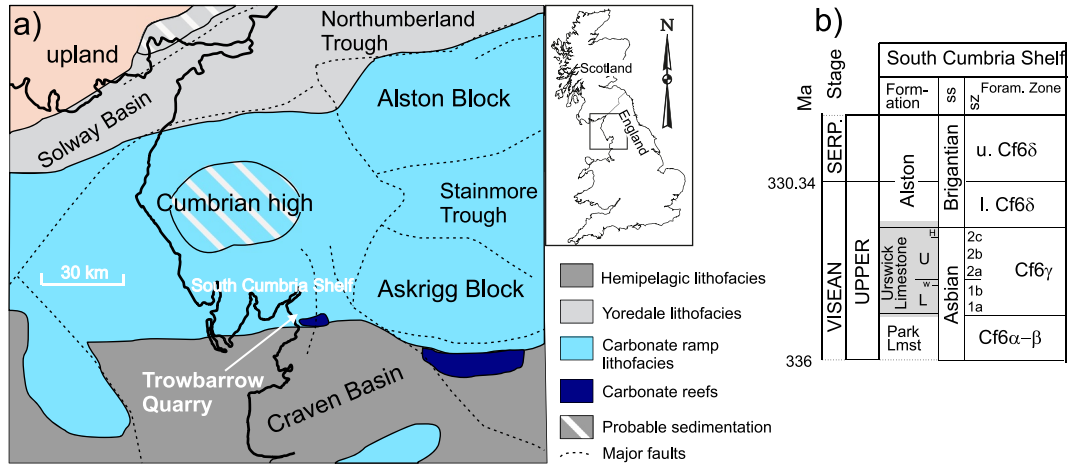

Figure 1. (a) Paleogeographic map of NW England for the late Asbian (modified from Wakefield et al. (2016)), with the study site at Trowbarrow Quarry indicated. (b) Simplified lithostratigraphy and foraminiferal biostratigraphy of the strata at Trowbarrow (from Cózar, Somerville, Hounslow, and Kamenikova (2022)), with the gray interval indicating the studied interval. L = lower, U = upper, H = Humphrey Head Limestone Member. W = Woodbine Shale. SERP. = Serpukhovian, SS = British substage, sz = sub-zonal foraminiferal assemblage.

been a key pacing metronome in cyclothem development (Davydov et al., 2010; Fang et al., 2022; Heckel, 2013). Eccentricity-driven change, particularly short eccentricity at the ~100 kyr period, seems to have been the primary driver for the shortest cyclothems, where in some areas these are grouped into longer cycles at the long eccentricity period of ~405 kyr (Davydov et al., 2012; Giles, 2009; Korn & Kaufmann, 2009; Montañez, 2022; Opluštil et al., 2022). Non-linear feedback mechanisms were also likely key in expanding the presence of the relatively weak Milankovitch forcing into the sedimentary archive (Huang et al., 2021; Meyers, 2019). Just as the late Cenozoic sea-level change driven by ice accumulation and melting was likely strongly asymmetric, due to more rapid melting than that of ice accumulation (Hays et al., 1976), likely distortion of the Milankovitch forcing signals probably occurred in shallow water sediments.

Given the parallels between the LPIA and the Cenozoic ice-house conditions, cyclostratigraphic studies are at the frontier of developing 10–100 kyr resolution age models for Carboniferous strata. Relatively few Pennsylvanian cyclostratigraphic studies have used robust statistical methods for astronomical period identification (Montañez, 2022 lists six key studies), but have instead largely relied on essentially sequence stratigraphic cycle-counts paced to radioisotopic anchor points (Davydov et al., 2010; Heckel, 2013; Pointon et al., 2012). The Mississippian has even fewer quantitative cyclostratigraphic studies, since many of the better-studied successions are low paleolatitude, shallow water carbonate systems, which express cyclicity in differing ways to cyclothems (Cózar, Somerville, Hounslow, & Coronado, 2022; Wright et al., 1997). Also, for low paleolatitude sites, unraveling the impact of cyclical changes in climate driven by probable superimposed monsoonal and ice-volume changes in the Carboniferous is a complex problem (Opluštil et al., 2022).

Shallow marine carbonates, whilst sensitive to sea-level change also have a number of internal processes which can generate repetitive (i.e., autocyclic) changes in facies, which may have little or no connection to astronomical forcing (Strasser, 2018). It is therefore particularly important to understand the processes that controlled sedimentation and the climatic proxies in carbonate systems (Da Silva et al., 2013). Strasser (2018) suggested three key conditions for the preservation of astronomically driven cycles in shallow marine carbonates: (a) sufficient accommodation space allowing avoidance of prolonged exposure, (b) high sedimentation rates to avoid condensation, and (c) paucity of high-energy events destroying prior deposits. The Middle Mississippian (Asbian) study section used is at Trowbarrow Quarry in NW England (Figure 1a), which has a well-defined foraminiferal biostratigraphy, which acts as a reference section for this substage interval (Cózar, Somerville, Hounslow, & Coronado, 2022; Cózar, Somerville, Hounslow, & Kamenikova, 2022) and as we show, has a moderate accumulation rate. Carbonate cycles at Trowbarrow (Horbury, 1987) are distinct from the classic "Yoredale," carbonate–clastics–coal-type cyclothems (Fielding et al., 2008) and are here referred to as rhythms, following Davies (1982) and Cózar, Somerville, Hounslow, and Coronado (2022). The term "cycle" is used here to refer to

25724525, 2024, 3, Downloaded from https://agupubs.onlinelibrary.wiley.com/doi/10.1029/2023PA004772 by Spanish Cochrane National Provision (Ministerio de Sanidad), Wiley Online Library on [02/04/2024]. See the Terms and Conditions (https://onlinelibrary.wiley.com/terms-and-conditions) on Wiley Online Library for rules of use; OA articles are governed by the applicable Creative Commons License

25724525, 2024, 3, Downloaded from https://agupubs.onlinelibrary.wiley.com/doi/10.1029/2023PA004772 by Spanish Cochrane National Provision (Ministerio de Sanidad), Wiley Online Library on [02/04/2024]. See the Terms and Conditions (https://onlinelibrary.wiley.com/terms-and-conditions) on Wiley Online Library for rules of use; OA articles are governed by the applicable Creative Commons License

other kinds of non-carbonate repetitive patterns. The late Asbian is at the transition from the greenhouse to sustained ice-house conditions of the later Carboniferous.

This study focuses on unraveling the nature of cyclicity in upper Asbian shallow marine carbonates, by using a combination of petrographic study, rock magnetic proxies and astrochronological testing. Rock magnetic proxies have been widely used in astrochronologic studies, since the measurements are relatively quick, precise, and cheap, and can be applied at almost any sampling scale (Kodama & Hinnov, 2014). In carbonate-dominated successions, rock magnetic proxies often largely reflect the Fe and Fe-oxide content, which is often largely associated with the siliciclastic fraction (Da Silva et al., 2009; Hladil et al., 2006), and is primarily diluted by $CaCO_3$ generated by the carbonate factory. It is therefore important to understand the linkages between the mineral magnetic proxies and the carbonate components, which express the dominant rhythmic and environmental components of carbonate systems. Within this context, our work: (a) Determines which magnetic minerals carry the magnetic proxies, and their probable sources and origins. (b) Evaluates the associations between the magnetic proxies, the carbonate components and inferred environmental conditions, so informing how the magnetic proxies may be reflecting depositional environment. (c) The prior steps inform how the magnetic proxies may be expressing any astronomically driven environmental changes. (d) Finally, the magnetic proxies are used to determine an astrochonology in the late Asbian interval at Trowbarrow.

2. Study Area and Rhythms in the Late Asbian

The study area is located on the southern flank of the Lake District (Cumbrian) high, which acted as persistent upland feature during the Early Mississippian (Tournaisian), but was likely drowned near the start of the Middle Mississippian (Visean) (Adams et al., 1990). This region of south Cumbria (the South Cumbria Shelf, SCS; Figure 1a) permitted accumulation of about 640 m of carbonate-dominated sediments from the uppermost Tournaisian to the early Brigantian (Johnson et al., 2001). During the late Asbian, sedimentation was coeval with carbonate ramp and reef sediment deposition to the east on the Askrigg Block and passed southwards into deeper-water shale-dominated units in the Craven Basin (Figure 1a). This ~80 km N-S transition, from the Scottish borders is a mixed carbonate-clastic ramp (Mount, 1984; Thurlow, 1996), comparable in scale to similar well-known systems that formed in the Neogene (Dunbar et al., 2000; Viera et al., 2019). This study is largely focussed on the Urswick Limestone Fm (ULF), although sampling overlaps into the lowest part of the overlying Alston Fm, as well as the uppermost few meters of the underlying Park Limestone Fm (Figure 1b). The ULF is subdivided into the lower ULF (including the Woodbine Shale in its upper part) and upper ULF (with Humphrey Head Limestone Member in its upper part; Figure 1b).

Like other upper Asbian (late Visean) carbonate ramps in Britain and elsewhere in Europe (Gallagher, 1996; Gray, 1981; Schwarzacher, 1961; Somerville, 1979b; Vanstone, 1993; Walkden, 1974), the ULF shows pronounced cyclic changes in a number of ways. Firstly, the ULF is punctuated by emergent surfaces, sculptured by paleokarsts and sometimes with overlying silty, poorly consolidated terrestrial deposits, or thin laminated calcretes and rootletting, representing paleosols (Horbury, 1989; Vanstone, 1998; Walkden, 1974). The karstified surfaces and the terrestrial sediments may be reddened in some cases (Mitchell, 2004, p. 93). These terrestrial intervals may only have limited duration, evident by the immaturity of late Asbian paleosols (Vanstone, 1996). Secondly, the lithologic variation within the rhythms may be broadly organized into basal wackestone-packstone intervals with overlying grainstones, with the basal parts in some cases being more argillaceous. These broadly reflect upward-shallowing cycles, from sub-tidal or below fair-weather wave base conditions to in some cases supratidal environmental conditions (Figures 2b and 2c). Other British and Irish regions display similar rhythmicity (Cózar & Somerville, 2005; Davies, 1982; Gallagher et al., 2006; Gray, 1981; Somerville, 1979a; Vanstone, 1996). Thirdly, allochem assemblages may be similarly organized into intervals reflecting these deeper-shallower environmental changes like those envisaged by Horbury (1987; Figure 2) or Horbury and Adams (1996). Other regions of late Asbian carbonates may differ in their allochem contents to the ULF, but show a similar style of organized behavior (Cózar & Somerville, 2005; Davies, 1982; Gallagher, 1996; Giles, 2009; Kabanov et al., 2016). Fourthly, species and genera diversity in foraminifera may also display cyclical changes (Cózar, Somerville, Hounslow, & Coronado, 2022), perhaps responding in a similar same way to the forcing evident by differing allochem assemblages. These and the foraminifera sub-zonations provide a means to subdivide the succession at Trowbarrow into major emergent surfaces (O to XII; Figure 3a) that can be widely correlated and related to intervals of rhythms which are bounded by these major surfaces (labeled Rh1 to Rh 13; Figure 3a). We refer to an interval between these major emergent surfaces as an emergent-interval. Fifthly, we

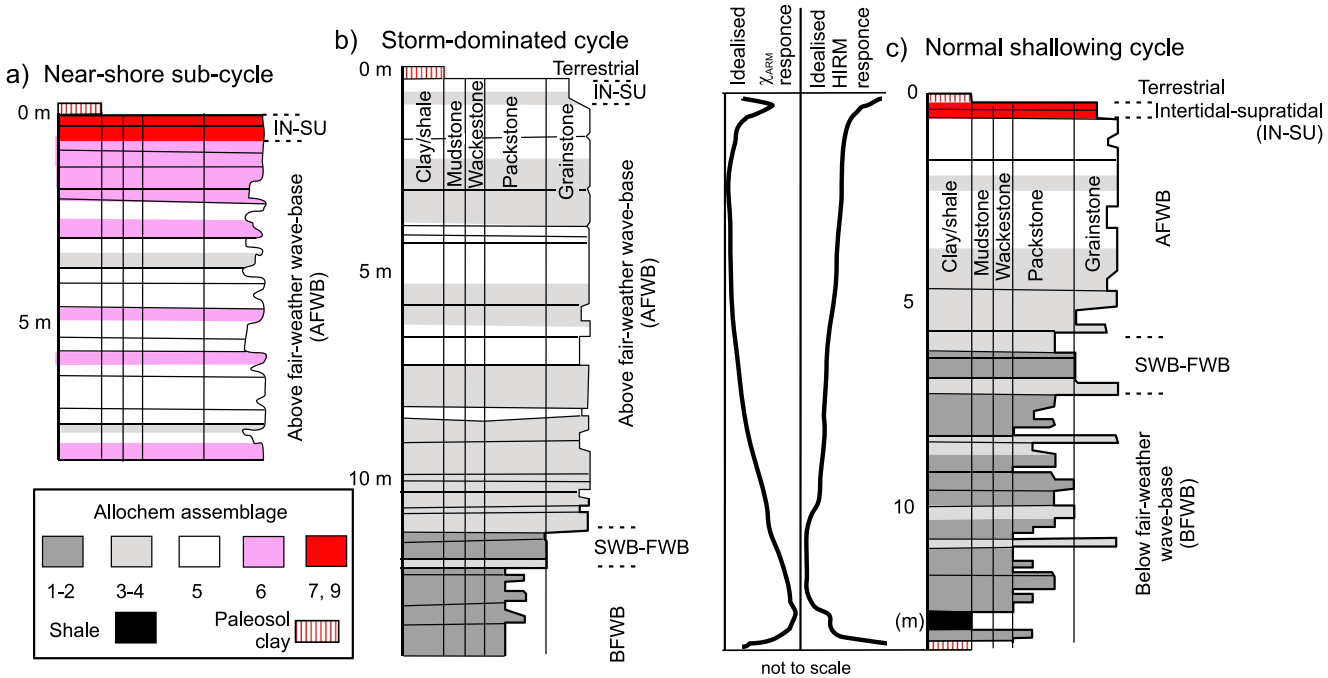

Figure 2. Idealized rhythms in the lower ULF, reflecting (a) near-shore, (b) a storm-dominated (high-energy) cycle, (c) a typical upwards shallowing cycle (simplified from Horbury, 1987). Shown in (c) are the idealized changes in the magnetic proxies for magnetite and hematite (χ_{ARM} and HIRM respectively), as discussed in the text. FWB = fair-weather wave-base, BFWB = Below FWB, SWB = storm wave-base, AFWB = above FWB. IN-SU = intertidal- supratidal. Dominant components in allochem assemblages from Horbury (1987) are: 1 = sponge spicule + bivalve + *Coelosporella* + gastropods; 2 = *Kamaenella* + foraminifera + calcispheres; 3 = like 2, but with abundant small peloids and micritic clots. 4 = dominance of *Kamaenella* over all others. 5 = small peloids and *Kamaenella* dominate. 6 = presence of large micritised grains, with peloids and *Kamaenella* less abundant than in 4 and 5. 7 = abundance of peloids over all other allochems. 8 = oolitic grainstones (barely present in the Trowbarrow section). 9 = small coalesced peloids and minor bioclasts of calcispheres and *Kamaenella*.

demonstrate here that magnetic measurements provide proxies for the clastic fraction, and express an alternative, but related cyclicity to the carbonate rhythms at Trowbarrow.

3. Samples and Methods

Samples from Trowbarrow were of two types; firstly, sub-samples from the oriented samples described by Cózar, Somerville, Hounslow, and Kamenikova (2022) and Hounslow et al. (2024) at a mean spacing of 1.1 m, and secondly, smaller chip-samples collected at ~25 cm spacing between the oriented samples. The samples at a mean spacing of 1.1 m were classified into microfacies and inferred environmental conditions (Figures 3d and 3e) based on 480 thin sections using the classifications of Embry and Klovan (1971), Wright (1992), and Flügel (2004). In addition, using the base-mid-top, depth-based allochem classification (referred to here as Horbury and Adams Classification, "HAC rhythms") of Horbury and Adams (1996), our samples are classified into HAC rhythms in Figure 3c, with inferred shallowing-up cycles from Cózar, Somerville, Hounslow, and Coronado (2022). Also, the environmental and allochem assemblages for the Trowbarrow section from Horbury (1987) were mapped onto our depth scale (Figure 3b), along with the inferred shallowing cycles using the idealized rhythms in Figure 2 and shown in Figure 3b.

3.1. Magnetic Proxies

Magnetic measurements were performed on the core plug samples at ~1.1 m spacing and the ~25 cm spaced rock chips. The chip samples were carefully selected and cleaned to avoid surface contamination (e.g., soil, lichen) from the outcrops. Combining both sets of samples the overall median spacing was 26 cm for the section, with the detailed sample positions indicated in Figure S1 in Supporting Information S1. To prepare the chip-samples for magnetic measurements they were pelletized in a jaw crusher, and a sub-sample was packed into plastic pots. To stabilize the pellets in the pots a small amount of PVA glue was used to bond the fragments together, and subsequently dried at 40°C. The set PVA glue used had small residual magnetisations similar in scale to that from the

25724525, 2024, 3, Downloaded from https://agupubs.onlinelibrary.wiley.com/doi/10.1029/2023PA004772 by Spanish Cochrane National Provision (Ministerio de Sanidad), Wiley Online Library on [02/04/2024]. See the Terms and Conditions (https://onlinelibrary.wiley.com/terms-and-conditions) on Wiley Online Library for rules of use; OA articles are governed by the applicable Creative Commons License

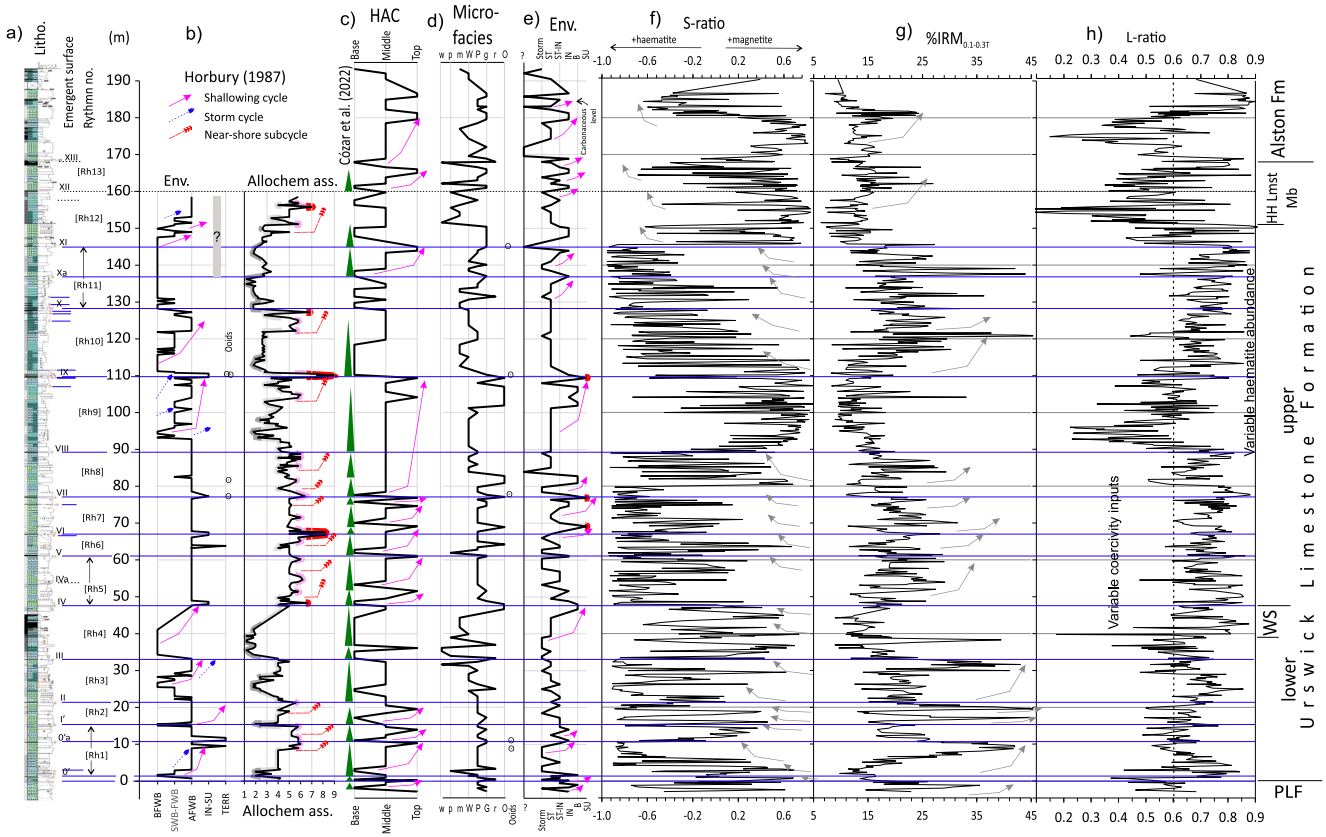

Figure 3. Comparison of magnetic mineral proxies and cycle/rhythm data for Trowbarrow. (a) lithologic log and emergent surface (in blue) codes (0' to XIII) and rhythm number (Rh1 to Rh13 inside []) from Cózar, Somerville, Hounslow, and Kamenikova (2022). Minor emergent surfaces also indicated with short lines. Dotted line indicates prominent bedding feature inferred to correlate to emergent surface elsewhere (Cózar, Somerville, Hounslow, & Coronado, 2022). (b) Summary allochem associations from Horbury (1987), with idealized shallowing-up cycles as in Figure 2 (sub-class of main allochem association is ±0.2* the subclass code, for higher (+) or lower (−) sub-class). Environment (Env.) and allochem codes as in caption to Figure 2, with ooid-bearing samples indicated with Θ. Color on allochem data is that from Figure 2 emphasizing the association between cycles and allochems. Grayed interval at 145–160 m indicates this part of Horbury's data set is not securely tied to our sampling and log. (c), (d), (e) Petrographic data from our sampling, with inferred shallowing-up cycles in the HAC (Horbury and Adams Classification) data and environment inferred. Microfacies codes: *w* = argillaceous-wackestone, p = argillaceous packstone, m = mudstone, W = wackestone, P = packstone-grainstone, G = grainstone, r = rudstone, O = microbial. Environment code: ? = uncertain, Storm = tempestite, ST = sub-tidal background, ST-IN = intertidal-subtidal, IN = intertidal, B = boundstone, SU = supratidal, ooid-bearing samples indicated with Θ. (f), (g), (h) magnetic mineralogy proxies, utilizing the full sampling set. Gray arrows on F and G represent inferred trends in the magnetic data, as indicated in Figure 4 and the text. Lithostratigraphic abbreviations and labeling on (h) as in Figure 4.

plastic pots. Multiple suitable blanks were also prepared and measured in the same way to allow removal of the magnetic properties of the encapsulating materials and PVA from the specimen data.

The methods used to determine the rock magnetic data set are detailed in Supporting Information S1, and details about the magnetic proxies used are summarized in Table 1 and the data sets are in Hounslow et al. (2023).

3.2. Astrochronologic Testing

The astrochronologic analysis used a phased approach, firstly by testing the data set for likely astronomical signals based around spectral analysis methods, and secondly developing a sedimentation rate model using a triangulation-approach as advocated by Meyers (2019). The key steps in this analysis were:

1. Spectral peak identification using the LOWSPEC method (Meyers, 2012), which attempts to resolve some of the issues with peak identification highlighted by Weedon (2022a). A 95% confidence cut-off was used with LOWSPEC and a time-bandwidth product of three. Data was pre-conditioned by detrending and Box-Cox transformations, and for the LOWSPEC method the spectral peaks were pooled from several interpolation intervals, and averaged using kernel density estimates. Details of these methods are in Supporting Information S1.

25724525, 2024, 3, Downloaded from https://agupubs.onlinelibrary.wiley.com/doi/10.1029/2023PA004772 by Spanish Cochrane National Provision (Ministerio de Sanidad), Wiley Online Library on [02/04/2024]. See the Terms and Conditions (https://onlinelibrary.wiley.com/terms-and-conditions) on Wiley Online Library for rules of use; OA articles are governed by the applicable Creative Commons License

25724525, 2024, 3, Downloaded from https://agupubs.onlinelibrary.wiley.com/doi/10.1029/2023PA004772 by Spanish Cochrane National Provision (Ministerio de Sanidad), Wiley Online Library on [02/04/2024]. See the Terms and Conditions (https://onlinelibrary.wiley.com/terms-and-conditions) on Wiley Online Library for rules of use; OA articles are governed by the applicable Creative Commons License

Table 1
Summary of the Magnetic Variables Used, Indication of What They Provide as a Physical Proxy in This Study and Type of Detrending Used on the Box-Cox Transformed Values

Magnetic variable	Proxy for:	Type of detrending
χ_{LF}	Abundances, here of Fe-bearing silicates + carbonates + Fe-oxides	Linear
χ_{ARM}	Fe-oxide abundance, sensitive to ultra-fine-grained magnetite	Polynomial
SIRM	Fe-oxide abundance	Polynomial
HIRM	Fe-oxide abundance, sensitive to hematite and partly goethite	Polynomial
IRM_{40mT}	Fe-oxide abundance, sensitive to coarser-grained magnetite	Polynomial
$\%IRM_{0.1\text{-}0.3T}$	Hematite to magnetite ratio and/or proportion of finer-grained magnetite	Polynomial
S-ratio	Hematite to magnetite ratio when in mixtures (Frank & Nowaczyk, 2008)	Polynomial
L-ratio	Coercivity-concentration dependency in hematite- goethite (Liu et al., 2007) and/or magnetite proportions.	Polynomial
abun.PCA1	Principal component of χ_{ARM}, IRM_{40mT}, HIRM and $\chi_{LF,}$ so a collective abundance indicator	Polynomial
min.PCA1	Principal component of S-ratio, $\%IRM_{0.1–0.3T}$, %HIRM, and the L-ratio, so a kind of mineralogy—mixture indicator	Polynomial

Note. %HIRM = 100*(HIRM/SIRM). Further details about magnetic variables can be found in Peters and Thompson (1998), Walden (1999), Peters and Dekkers (2003), and Kodama and Hinnov (2014).

2. Testing spectral peaks against astronomical targets using the average spectral misfit (ASM) technique (Meyers & Sageman, 2007).
3. Devising plausible sedimentation accumulation rate (SAR) models for the succession using the TimeOpt methodology (Meyers, 2015), evolutionary TimeOpt (Meyers, 2019; Sinnesael et al., 2021), and timeOptTemplate procedures. The multiple proxies allowed triangulation and testing of the SAR models using the TimeOpt regression coefficients $r^2_{envelope}$ and r^2_{opt} (Meyers, 2015), where r^2_{opt} is the expression of the amplitude envelope*spectral power. This approach progressed from simple linear SAR models toward two more complex models which included hiatus. The data set here seems to correspond to a category which has high values of lag-1 autoregressive noise (large σ_{AR1}) and high noise to signal ratios. With this category of data, the $r^2_{spectra}$ estimates offer less powerful means of elucidating astronomical forcing (Meyers, 2015), so $r^2_{envelope}$ and r^2_{opt} are preferentially used here.
4. The duration of the late Asbian and its uncertainty was determined using the three better astronomically forced proxies and two equally likely SAR models which included three significant hiatuses in the models.

For steps 2 to 4 eccentricity and precession astronomical targets for 333 Ma were determined using the fundamental secular frequencies (g_1 to g_5, precession rate k) estimated by linear interpolation of the data in Zhou et al. (2022) and Meyers and Malinverno (2018). These were converted to periods using the astrochron package (Meyers, 2014), with the used periods and interpolations shown in Table S1 and Figure S4 in Supporting Information S1. Obliquity periods at 333 Ma used those of Waltham (2015). For ASM, we excluded spectral peaks with less than five sampling points defining them, as suggested by Kemp (2016). With the median sample spacing of 0.26 m, this is a frequency of 0.96 cycles/m so an overall 1 cycle/m was used for this cut-off. The astrochronologic analysis was performed in R (R Core Team, 2013) largely using astrochron v1.1 (Meyers, 2014).

4. Results: Relationships Between Magnetic and Carbonate Data Sets

Since rock magnetic data sets do not necessarily provide ideal proxies for paleoclimatic data, we first examine the key environmental characteristics of the carbonate system in the ULF at Trowbarrow, and then go on to examine the relationship between the carbonate data set and the magnetic proxies. This essential step is important in demonstrating how the magnetic proxies respond to the carbonate system and their likely environmental forcings, and which of the magnetic proxies may be better expressing these forcings.

4.1. Carbonate Lithofacies and Cycle-Relationships

There is a good degree of correspondence between microfacies and environmental observations and interpretations between our sampling and that of Horbury (1987), although there are also some differences due to

25724525, 2024, 3, Downloaded from https://agupubs.onlinelibrary.wiley.com/doi/10.1029/2023PA004772 by Spanish Cochrane National Provision (Ministerio de Sanidad), Wiley Online Library on [02/04/2024]. See the Terms and Conditions (https://onlinelibrary.wiley.com/terms-and-conditions) on Wiley Online Library for rules of use; OA articles are governed by the applicable Creative Commons License

sampling density/position and petrographic classifications. The observations of Horbury (1987) are more focussed on the microbially-induced facies at the emergent surfaces, than our sampling.

Rudstone and microbially induced microfacies are important in defining rhythm tops in the lower ULF, whereas in the upper ULF, emergent surfaces IV to IX typically have HAC rhythm tops important in defining the topmost terminations (Figures 3b–3d).

In the lower parts of the upper ULF, supratidal facies and microbial microfacies are important for defining rhythm tops in the emergent surface interval IV to IX interval, and in the interval IX—XII the intertidal facies or HAC—top facies define rhythm tops (Figures 3b and 3d).

The microfacies immediately overlying the paleosols and emergent surfaces are quite variable, in spite of the sudden deepening, as envisaged in the idealized model in Figure 2c. Horbury and Adams (1996) modified these models to include an ooid-bearing facies in the earliest transgression phase following the terrestrial facies. This ooid-bearing facies was envisaged as deposited on the front of the distal ramp at the sea-level lowstand, but with this facies largely missing from mid-ramp sections. However, this initial transgressive phase is represented in ooid-bearing levels immediately following emergent surfaces O'a, VII, IX, and XI (Figures 3b and 3d).

Subsidiary rhythms occur in the IV–VIII interval, indicating that whilst rhythms Rh1-Rh13 appear the dominant metronome, other lower order features are also present. Some of these may relate to minor emergent surfaces (i.e., IVa in Rh5, and intervals in Rh7 and Rh10; Figures 3a–3c).

Some rhythms (e.g., Rh1, Rh2, Rh4, Rh10) are distinctly asymmetric in facies, that is, deeper facies low in the rhythm interval, but others (e.g., Rh3, Rh5, Rh6, Rh7, Rh8, Rh9, Rh11, Rh12) are less so, and deepest water environments may be in the mid-parts of the rhythm (Figures 3b and 3e). The asymmetry in accumulation as implied by the idealized rhythms in Figure 2 is therefore not universal.

A key point is that there are both primary and superimposed subsidiary rhythm responses in some intervals, but less so in others. Hence, there is not just one cyclic pacing to the carbonate factory changes or the sea-level drops expressed by the emergent surfaces. Naturally, this is the reason that not just one type of "idealized cycles" can be observed. If Milankovitch-type forcing were pacing the carbonate cycles this would make sense, since the carbonate signal could be a composite of eccentricity, obliquity and precession-driven forcing. Also, a pure astronomical signal is unlikely to be present, since glacioeustasy (impacted by ice-retreat and advance and melting), rates of subsidence, as well as autocyclic factors also have impact on the rhythms.

4.2. Controls on the Magnetic Proxies

The ferrimagnetic magnetic mineralogy is largely dominated by a mixture of hematite and magnetite, discussed at length in Hounslow et al. (2024). The hematite is not derived from mineralization, modern karstification or pyrite weathering, for the reasons outlined in Hounslow et al. (2024). This mixed mineralogy is most evident by the S-ratio which swings between −1 and ∼0.6 (Figure 3f), indicating contributions from hematite of between 99.9% and 90% relative to magnetite (mass content), if using estimates of Frank and Nowaczyk (2008). Hard isothermal remanent magnetization (HIRM) is strongly related to the saturation isothermal remanent magnetization (SIRM) (Table S2 in Supporting Information S1) with both largely reflecting the hematite abundance. The L-ratio suggests that above a HIRM of $\sim 10 \times 10^{-7}$ Am^2/kg the abundance of hematite is a primary control on the HIRM, whereas below this threshold (Liu et al., 2007; Figure 3h), the HIRM is likely controlled by variable mixtures and abundances of both magnetite and hematite with possibly differing coercivity of hematite (Figure 4d). Because of the ∼30-fold and ∼700-fold larger SIRM and χ_{LF} of magnetite over hematite (Peters & Dekkers, 2003), magnetite is preferentially expressed in many of the magnetic proxies in comparison to its minor mass contribution.

The magnetite fraction is largely associated with a detrital fraction connected with the marine clastic mudstone in the sections, evident by the consistently larger values of χ_{ARM} and IRM_{40mT} in the Woodbine Shale, and clastic-rich intervals in the Alston Fm (Figures 4b and 4c). The magnetite fraction appears to be as both discrete grains (Hounslow et al., 2024), but may also contain magnetite included in silicates, such as quartz and feldspar, which are relatively immune to diagenetic modification (e.g., Franke et al., 2007; Hounslow & Maher, 1996; Jiang et al., 2021). These magnetite-abundance driven changes are largely disconnected from the hematite abundance (shown by the HIRM; Table S2 in Supporting Information S1), except in the Alston Fm, where the connection is slightly stronger (compare Figures 4d and 4b). Likewise, χ_{LF} has a similar response, since it is more strongly

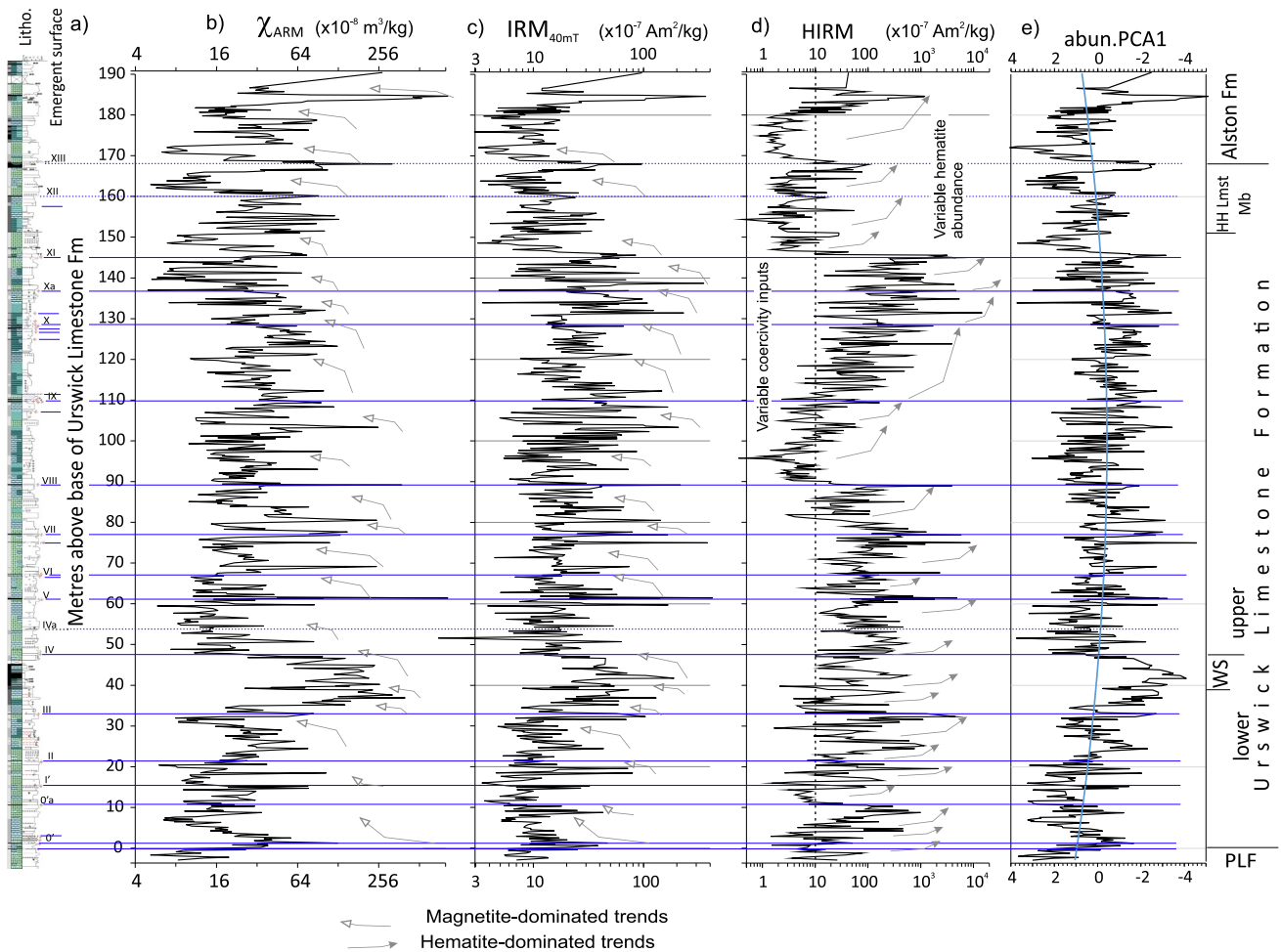

Figure 4. Comparison of the magnetic mineral abundances proxies, χ_{ARM}, IRM_{40mT}, HIRM against the: (a) log and emergent surfaces in the section (labeled as in Cózar, Somerville, Hounslow, and Kamenikova (2022)). Emergent surfaces which are not seen in the Trowbarrow section but are emergent at other correlated sections in the UK and Ireland are dotted. Minor emergent surfaces shown with short line. Arrows in (b), (c), (d) indicate the inferred magnetite- and hematite-dominated trends in the magnetic proxy data. Labels in (d) derived from inference based on the HIRM to L-ratio relationship as in Liu et al. (2007). Quadratic fitted (blue line) in (e) is illustrative of that used to make proxies stationary for astrochronologic testing. PLF = Park Limestone Formation, WS = Woodbine Shale, HH Lmst Mb = Humphrey Head Limestone Member.

related to χ_{ARM} and IRM_{40mT} (Table S2 in Supporting Information S1), than high field abundance proxies (i.e., SIRM, HIRM) which are most strongly reflecting the hematite component. The χ_{LF} may also reflect abundance of Fe-silicates (e.g., chlorite) in the detrital fraction, since χ_{LF} typically shows a stronger response than χ_{ARM} and IRM_{40mT} over those intervals richer in siliciclastics (Figure S2 in Supporting Information S1).

To determine the likely controls on the siliciclastic-driven magnetic signal, the set of "end-member" type samples is preferentially displayed over the fields occupied by the whole sample set in Figure 5. The shale samples have consistently larger χ_{ARM} and χ_{LF} (Table 2), with the bulk of the remaining samples having considerably lower values due to carbonate dilution (Figures 5a and 5c). Highly argillaceous wackestone samples also have elevated χ_{ARM} and χ_{LF} compared to the two main clusters of samples (two clusters separated by a dashed-line in Figures 5a and 5c; Table 1). Shale and argillaceous wackestone samples fall into two clusters (S and A in Figure 5), with the S-cluster having lower S-ratios than the A-cluster. The A-cluster consists of samples from the Woodbine Shale (with one from the Alston Fm). It is possible these two clusters may relate to a provenance difference in the marine siliciclastics (i.e., larger content of hematite in the S cluster; Figure 5d), although more work needs to be done to validate this speculation.

The few samples from the paleosols indicate that these are much enhanced in hematite, with generally larger HIRM and SIRM and lower S-ratio (Table 2; Figure 5d). Some samples proximal to emergent surfaces have

25724525, 2024, 3, Downloaded from https://agupubs.onlinelibrary.wiley.com/doi/10.1029/2023PA004772 by Spanish Cochrane National Provision (Ministerio de Sanidad), Wiley Online Library on [02/04/2024]. See the Terms and Conditions (https://onlinelibrary.wiley.com/terms-and-conditions) on Wiley Online Library for rules of use; OA articles are governed by the applicable Creative Commons License

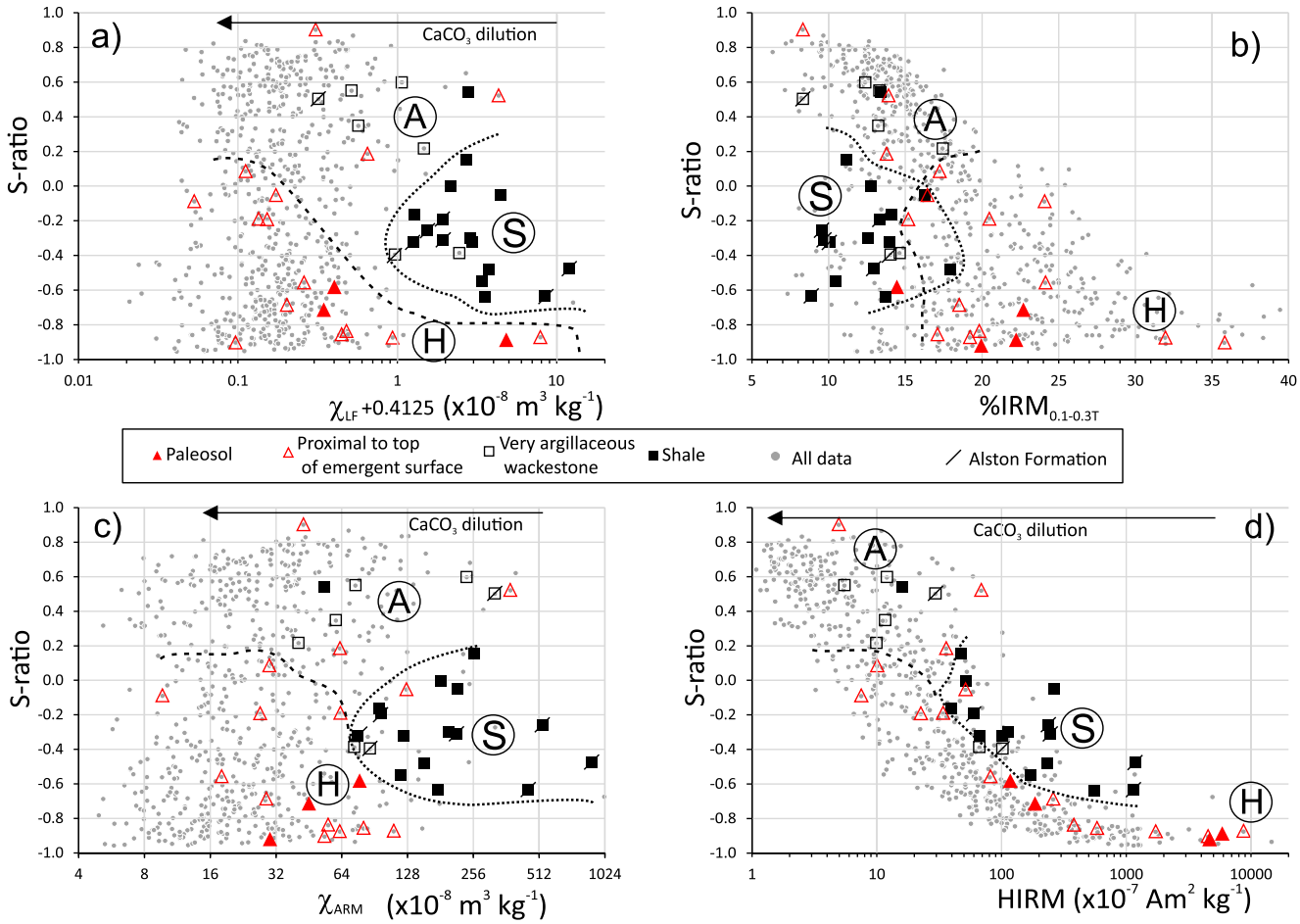

Figure 5. Magnetic parameter bi-plots of all the samples, with the subset for clastic groups as in Table 2, emphasized with additional symbols. -A-, -H- and -S- are clusters of samples which correspond to very argillaceous wackestones, hematite-rich paleosols, and shale samples respectively. (a), (c), and (d) are magnetic mineral abundance proxies, and hence dilution by diagenetic carbonate will lower this proxy according to the arrows indicated at the top. Pure calcite has a χ_{LF} of -0.446×10^{-8} m^3/kg (Schmidt et al., 2006) and would plot at -0.03×10^{-8} m^3/kg on the scale in (a).

similar magnetic properties to the paleosols (Figure 5), suggesting a similar magnetic mineralogy. The paleosols have lower contents of fine-grained magnetite compared to the marine-clastics, if using χ_{ARM} for comparison (Table 2; Figure 5c). In contrast, the magnetite contents using the IRM_{40mT} proxy suggests softer (i.e., larger sized) magnetite may be elevated in abundance in the paleosols (Table 2). The parameter $\%IRM_{0.1–0.3T}$ also seems to approximately distinguish the bulk of the marine siliciclastics from the paleosol-related sources (Table 2; Figure 5b). This distinct contrast between paleosol-clastics and marine-derived clastics accords with XRD mineralogy data of Walkden (1972) and Somerville (1977) who indicated larger amounts of mixed layer illite-smectite, lower quartz and carbon contents and elevated Zr, Rb, and anatase in Asbian paleosol levels, compared to normal background siliciclastics. This silicate mineralogy difference has been confirmed more widely in other Asbian carbonates in Britain, and minor mixed kaolinite-smectite contents have also been detected indicating possible paleosol origins or derivation from in situ processes (Vanstone, 1993, 1998). Paleosols from the lower ULF have clay contents of illite ≅ 48%, kaolinite ≅ 15%, interlayered illite-smectite, kaolinite-smectite and chlorite-smectite of ≅30, 5%, and 5% respectively (Vanstone, 1993). Although the illite-smectite content may largely be a function of burial depth (Burnett, 1987; McIntosh et al., 2021). An eolian source of British Asbian paleosol clastics has been generally accepted, although a primarily volcanic-origin of the high-smectite contents in the dusts seems unlikely considering their coincidence with emergent surfaces. This is borne out by the sparse contents of Visean age zircons in Asbian paleosols in Ireland (Pointon, 2012). Asbian paleosols are also relatively immature and show little geochemical or mineralogical evidence of pedogenic profile development (Vanstone, 1993), so the magnetic mineralogy was probably little impacted by pedogenic modification.

25724525, 2024, 3, Downloaded from https://agupubs.onlinelibrary.wiley.com/doi/10.1029/2023PA004772 by Spanish Cochrane National Provision (Ministerio de Sanidad), Wiley Online Library on [02/04/2024]. See the Terms and Conditions (https://onlinelibrary.wiley.com/terms-and-conditions) on Wiley Online Library for rules of use; OA articles are governed by the applicable Creative Commons License

Table 2
Medians of Representative Magnetic Parameters For the Clastic-Related Groups of Samples (These Use Both Sample Sets, but Predominantly the Chip-Set), Allochem Groups, the Inferred Environment (From Microfacies Data), and Microfacies

Grouping type	HIRM × 10^{-7} Am^2/kg	SIRM × 10^{-7} Am^2/kg	χ_{ARM} × 10^{-8} m^3/kg	IRM_{40mT} × 10^{-7} Am^2/kg	S-ratio	$\%IRM_{0.1-0.3T}$	χ_{LF} × 10^{-8} m^3/kg	*n*
Clastic groups								
Paleosol	4,664	6,098	38	73	−0.89	22.2	0.88	3
Underlying emergent surface	69	146	56	36	−0.19	18.5	−0.15	15
Very argillaceous wackestone	12	76	74	23	0.35	13.3	0.55	7
Shale	67	178	153	41	−0.26	13.2	1.76	16
Allochem groups								
HAC-Top	89	194	31	18	−0.65	16.1	−0.29	21
HAC-mid	34	87	22	13	−0.44	18.0	−0.30	105
HAC-bot	32	93	34	18	−0.45	15.3	−0.28	48
Environment								
Supratidal	167	263	133	49	−0.58	15.6	−0.15	3
Boundstone	25	74	18	19	−0.25	17.5	−0.26	11
intertidal	30	61	18	10	−0.51	15.7	−0.33	26
Subtidal-intertidal	68	150	25	12	−0.45	18.1	−0.31	28
Sub-tidal	31	92	27	15	−0.40	17.9	−0.29	67
Microfacies								
Microbial (O)	45	126	47	22	−0.28	17.5	−0.25	16
Rudstone (r)	20	199	56	59	0.34	12.7	−0.15	6
Grainstone (G)-top & mid	79	114	24	13	−0.62	15.7	−0.32	17
Grainstone (G)-base	19	58	15	10	−0.51	15.7	−0.34	13
Packstone (P)	55	148	20	12	−0.62	19.9	−0.31	65
Wackestone (W)	40	81	28	13	−0.2	17.7	−0.29	30
Mudstone (M)	24	88	41	20	0.32	13.7	−0.29	15
Argillaceous packstone (p)	32	65	47	21	0.07	14.4	−0.29	6
Argillaceous wackestone (w)	42	143	94	49	−0.34	17.0	−0.25	6

Note. Samples underlying emergent surfaces were 0–25 cm below, with a median of 5 cm, below the surface. n = number of samples in group. Microfacies codes as in Figure 3. Grainstones are divided into base-, mid- and top-rhythm grainstones (rhythm divisions shown in SI data).

The surprising abundance of hematite (S-ratio values < 0) in many parts of the section (Figure 3f) is much more than could be anticipated by the distribution of visible reddening. The hematite is not related in a simple fashion to the emergent surfaces in the section, where reddening is commonly seen, instead the data show:

1. A number of secular changes in the section, evident by many negative S-ratio values, particularly in the interval between the IV–VII and IX–XI emergent surfaces, where hematite is enhanced in content (Figure 3f).
2. A general, but modest enhancement of hematite (e.g., HIRM, SIRM) in the younger parts of cycles with larger values in the supratidal, and HAC cycle tops (Table 2), but not to the extent seen in the paleosols. Medians with respect to microfacies groups also show this relationship, where mid- and top-rhythm grainstones having the larger median HIRM and lowest S-ratio (Table 2), microfacies which are typical of the younger parts of normal rhythms (Figure 2c). Grainstones from rhythm bases have low ferromagnetic-mineral abundance proxies (HIRM, SIRM, χ_{ARM}) but still relatively enhanced hematite (negative S-ratio; Table 2).

25724525, 2024, 3, Downloaded from https://agupubs.onlinelibrary.wiley.com/doi/10.1029/2023PA004772 by Spanish Cochrane National Provision (Ministerio de Sanidad), Wiley Online Library on [02/04/2024]. See the Terms and Conditions (https://onlinelibrary.wiley.com/terms-and-conditions) on Wiley Online Library for rules of use; OA articles are governed by the applicable Creative Commons License

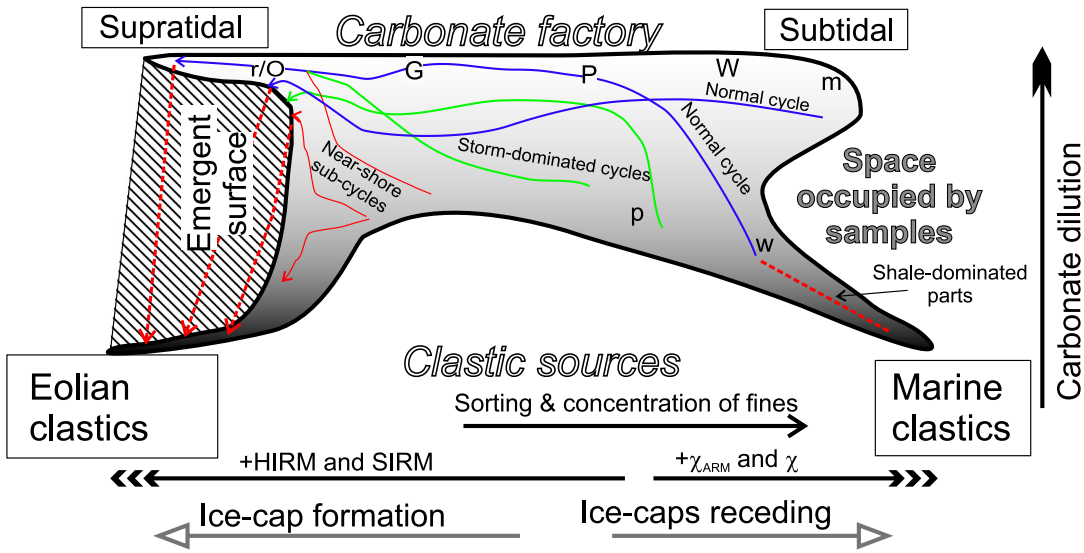

Figure 6. Conceptual model of the key controls on the magnetic variables, and how that maps onto the carbonate-based rhythms in the sections (as in Figure 2), which are largely driven by changes in the carbonate-factory systematics. Left and right indicate young and old limits of a single idealized cycle (as in Figure 2c). The thick borderline indicates the space occupied by the samples (not to any scale) with the hatched emergent surface representing absent information (no time-scale inferred). Labels w, p, m, W, P, G, r/O represent the diagrammatic position of microfacies categories in Figure 3d in this space. Magnetic proxies indicative of hematite and eolian-sources increase to the left and magnetite-and marine-sourced siliciclastics proxies increase to the right. The magnetic abundance proxies are modulated by increase in carbonate accumulation rates, which will cause dilution of the magnetic signal. Additional sorting and dispersal of fines from the grainstones and packstones will occur.

3. Of the samples within 25 cm of an emergent surface 47% have an S-ratio <−0.4%, and 13% have an S-ratio >0.4, indicating a preference for hematite proximal to emergent surfaces (Figure S5 in Supporting Information S1). However, not all the emergent surfaces are reddened (or have large HIRM; Figure 5d) and likely variable pyritization of paleosols and adjacent limestone surfaces has occurred, as observed elsewhere by Wright et al. (1997), which could have had a secondary impact on hematite (and perhaps magnetite) abundances below emergent surfaces.

In summary, the overall pattern of magnetic changes is assigned to two primary sources for the clastic fraction. First, a marine-derived fraction, richer in magnetite (larger χ_{LF}, χ_{ARM}, and $\%IRM_{0.1–0.3T} < \sim 16\%$; Figure 5b), that may be composed of two separate sources (the S and A groups in Figure 5). Second, an eolian-related fraction, much enhanced in hematite, which is distributed throughout the section, not just in the paleosols (Figure 5d). Within the carbonates, this fraction seems concentrated in the mid and upper parts of rhythms. When displayed with respect to the S-ratio, both χ_{LF} and $\%IRM_{0.1–0.3T}$ appear to be useful in providing a fair distinction of these clastic sources (Figures 5a and 5b). The eolian-derived fraction is inferred to be primarily derived from distal low-paleolatitude desert sources, probably on Laurentia to the west and northwest (Soreghan et al., 2023). This draws on similarity to Quaternary low-latitude dusts from Africa and some other major dust sources, which are likewise enriched in hematite, as measured by magnetic data sets (Doh et al., 1988; Hesse, 1997; Larrasoaña et al., 2015; Liu et al., 2012). Indeed, HIRM may be a useful proxy for eolian dust flux (Hesse, 1997; Larrasoaña et al., 2015; Figure 5d). In addition, eolian dusts make a major siliciclastic contribution to low-latitude carbonate banks at the present-day (Henrich & Hüneke, 2011; Muhs et al., 2012). The mixed-layer clay mineralogy and low quartz contents are also typical of the fines in eolian-sourced soils in present-day Bahamian carbonates (Muhs et al., 2012).

4.3. Relationship of Magnetic Proxies to Carbonate Rhythms

Carbonate-based facies and classifications are responsive to the carbonate factory systematics and wave and current sorting of carbonate grains on the ramp (Figure 6). In contrast, magnetic abundance proxies will respond particularly to factors external to the ramp, such as far-field eolian dust inputs, and delivery and dispersal from coastal siliciclastics, the most significant source of which was some 80 km to the north and NW (Figure 1a). However, even with a constant supply of siliciclastics with the same provenance, variable carbonate production rates will modulate the magnetic abundance proxies via dilution of the magnetic-mineral signatures

25724525, 2024, 3, Downloaded from https://agupubs.onlinelibrary.wiley.com/doi/10.1029/2023PA004772 by Spanish Cochrane National Provision (Ministerio de Sanidad), Wiley Online Library on [02/04/2024]. See the Terms and Conditions (https://onlinelibrary.wiley.com/terms-and-conditions) on Wiley Online Library for rules of use; OA articles are governed by the applicable Creative Commons License

Figure 7. The position of start and ends of trends in the magnetic data sets, with respect to the position (top, near-top, middle, near bottom and base) between emergent surfaces. Start (i.e., deep-end) for χ_{ARM}, IRM_{40mT}, S-ratio corresponds to high values, whereas that for HIRM are low values for the deep end of the trends. The shallow-end trends correspond to the converse of this. Gray and black bar colors indicate magnetite-dominated trends, and red and orange hematite dominated trends. These trends are those shown with arrows on Figures 3f, 3g, and 4b–4d. Only includes data between emergent surfaces O to XII (excluding surface IVa, and that above XII). (a), (b), (c) and (d) show the number of trends with respect to position for the deep-end and shallow end of the trends. (e) The cumulative number of trends between emergent surfaces, divided into type of magnetic proxy, and total number between each pair of emergent surfaces.

(Figure 6)—something which is difficult to directly infer without a detailed knowledge of sedimentation rates in the succession (but see below). The production-related carbonate dilution relationship will be modified by wave and current suspension and transfer of the siliciclastic silt and clay into lateral facies with a higher mud content, since magnetic minerals are largely concentrated in the fines (Thompson & Morton, 1979, Zheng et al., 1991; Razik et al., 2014.). The later response is broadly shown in the microfacies data with the lowest medians of χ_{ARM} and IRM_{40mT} in grainstones and packstone (G and P microfacies), and larger medians in argillaceous facies (p and w microfacies groups; Table 2). A similar but weaker response is shown by the medians for the intertidal to sub-tidal environmental divisions (Table 2). Therefore, in an idealized shallowing cycle these give a magnetite-based 'trend' displaying a younging-decrease in abundance proxies (χ_{ARM} and IRM_{40mT}) from a high in the shale and wackestone levels (Figure 2c). The abundance low corresponds broadly to the grainstone-packstone parts of these rhythms, since the uppermost parts show a larger χ_{ARM} and IRM_{40mT} due to increasing contributions from the eolian-derived siliciclastics in the upper parts of the rhythm (Table 2; Figure 2c). The clearly defined magnetite-dominated trends in the section are indicated in Figures 4b and 4c. Generally, these magnetite trends have a complex relationship with the major emergent surfaces in the section (Figures 4 and 7). One or two (and rarely 3) trends dominate between emergent intervals (Figure 7e), with the typical peaks (deep-end of the cycle) in the magnetite trends at the base to mid part, and lows in the magnetite-trend (shallowing-end) in the mid or upper parts of the emergent interval (Figures 7a and 7b).

The medians of χ_{LF} for the facies and environmental groups shows these magnetite-trends also, but with a much smaller change (Table 2). This is probably because χ_{LF} is relatively insensitive to the small amounts of siliciclastic content in these limestones (which are dominated by the susceptibility of calcite), and also that the lower ULF shows a strong secular decrease in χ_{LF} to the base of the ULF (Figure S2d in Supporting Information S1). Rudstone and microbial facies and supratidal environments likely have larger median magnetite abundance proxies (χ_{ARM}, IRM_{40mT}, and χ_{LF}) due to higher contents of eolian siliciclastics (Table 2).

Medians of the S-ratio with respect to the allochem and environmental groups show that HAC rhythm tops and supratidal environments have the largest relative contents of hematite (most negative S-ratios), with sub-tidal environments more positive S-ratios (Table 2). HIRM and SIRM also display larger values, showing more abundant hematite in the same divisions. These are inferred to designate hematite dominated-trends, the most

25724525, 2024, 3, Downloaded from https://agupubs.onlinelibrary.wiley.com/doi/10.1029/2023PA004772 by Spanish Cochrane National Provision (Ministerio de Sanidad), Wiley Online Library on [02/04/2024]. See the Terms and Conditions (https://onlinelibrary.wiley.com/terms-and-conditions) on Wiley Online Library for rules of use; OA articles are governed by the applicable Creative Commons License

25724525, 2024, 3, Downloaded from https://agupubs.onlinelibrary.wiley.com/doi/10.1029/2023PA004772 by Spanish Cochrane National Provision (Ministerio de Sanidad), Wiley Online Library on [02/04/2024]. See the Terms and Conditions (https://onlinelibrary.wiley.com/terms-and-conditions) on Wiley Online Library for rules of use; OA articles are governed by the applicable Creative Commons License

prominent of which are shown in Figures 4d and 3f. An idealized hematite-dominated trend displays a low HIRM near the base of the rhythm with increasingly larger values to the upper parts, and largest values in terrestrial and supratidal environments (Figure 2c). The section displays several differing kinds of relationships between emergent surfaces and trends (Figure 7). The largest HIRM's typify; (a) the uppermost beds below emergent surfaces I', III, VII, VIII, IX, and XI (Figure 4d), (b) the upper parts (but not uppermost) below emergent surfaces O'a, II, VII, X (Figure 4d), whereas (c) others have more than one trend between emergent surfaces (e.g., intervals below II, IV, XI surfaces). Highs in S-ratio (deep end of trend) occur near the base or middle of the emergent intervals (Figure 7d), and lows in S-ratio (shallow end) are most typical at or near emergent surfaces (Figure 7d). The hematite abundance proxy HIRM shows a similar relationship, although lows in HIRM typify the mid parts of emergent intervals (Figure 7c). $\%IRM_{0.1-0.3T}$ is also a useful discriminator of marine and eolian sources (Figure 5b), and similar trends are shown in this data set (Figure 3g), although not as clearly as HIRM and S-ratio.

In summary, a single, idealized deep to shallow cycle is therefore expressed in two key magnetic changes. Firstly, in the magnetic data as a magnetite-dominated trend of largely decreasing marine siliciclastics into the shallower-part of the cycle (Figure 2c). Secondly, a covarying hematite-dominated trend which increases toward the maximum of eolian-input in the paleosols (Figure 2c). Like in the Pleistocene and Neogene (Shin et al., 2021; Winckler et al., 2008; Zhang et al., 2020), we infer that eolian dust flux, using the HIRM proxy (or here alternative S-ratio or SIRM proxies), is primarily linked to increasing polar ice volume, and increasing atmospheric dustiness, which is why HIRM is closely related to the shallowing upper parts of the emergent intervals (Figure 6).

4.4. Radioisotopic Age Constraints on the Asbian Duration

To provide a window of likely average sediment accumulation rate (SAR) in the section we evaluated likely durations for the Asbian and late Asbian. The base of the Asbian is close to the base of the Belgium Warnantian Stage (Liu et al., 2023) and the base of the Warnantian is bracketed by radioisotopic dates of 335.6 and 336.2 Ma, so using a linear time-scale between these (Figure S11 in Supporting Information S1) gives the base of the Asbian as c. 336.12 ± 0.4 Ma (Pointon et al., 2014).

From the mid parts of the Belgium MFZ14 foraminiferal zone is radioisotopic date W13 of 332.5 ± 0.18 Ma (Pointon et al., 2014). The interval between the base of the late Asbian (approximately the base of MFZ14) to top of MFZ14 occupies the interval of the late Asbian to base Serpukhovian, which also includes most of the early Brigantian (Liu et al., 2023; Figure S11 in Supporting Information S1). Hence, date W13 is approximately at the base of the Brigantian, although a precise correlation cannot be made between the Belgium sections (where the equivalent to the late Asbian is ~10–12 m thick) and the base of the Brigantian at Trowbarrow. These correlated dates from Belgium suggest that the age range of the Asbian is c. 336.12–332.5 Ma, or about 3.62 ± 0.58 Myr in duration.

Assuming the base of the Asbian is around the middle of the Park Limestone Fm (125 m thick; Cózar et al., 2021), then the thickness for the Asbian nearby to Trowbarrow consists of 168 m of the ULF and ~40–65 m of the upper part of the Park Limestone Fm, which gives an estimated average SAR of 6.2 cm/kyr (uncertainty interval 5.0–7.7 cm/kyr).

The base of the Russian Mikhailovian Stage can be approximately correlated to the base of the late Asbian in the Trowbarrow section (Cózar, Somerville, Hounslow, & Kamenikova, 2022). A radioisotopic date 02VD-0 of 333.87 ± 0.19 Ma (Schmitz & Davydov, 2012) from the Verkhnyaya Kardialovka section is at the base of bed 21-8. Following the revised conodont biostratigraphy and its placement with respect to the Mikhailovian Stage of Pazukhin et al. (2010), 02VD-0 is approximately in the base or lower parts of the late Asbian. Hence, using the above date from Belgium for the top of the Asbian suggests a late Asbian duration of ~1.37 ± 0.37 Myr, which gives an alternative likely average SAR of the ULF of 12.3 cm/kyr (uncertainty interval 9.7–16.8 cm/kyr). The radioisotopic date from the condensed Verkhnyaya Kardialovka sections is less securely correlated to the Asbian than the Belgium dates. Hence, extreme SAR estimates for the ULF may range between 5.0 cm/kyr to perhaps as high as 17 cm/kyr, but with the most likely range of ~6–12 cm/kyr.

Using the average SAR from the Belgium or Russian section dates, and the median sample spacing at Trowbarrow of 26 cm, gives a median duration between samples of ca. 4.3 to 2.1 kyr, respectively (or 1 m = 16.4 kyr or 8.1 kyr, respectively). This suggests the sample spacing is sufficient to detect the shortest precession cycle (~17.2 kyr period) without aliasing.

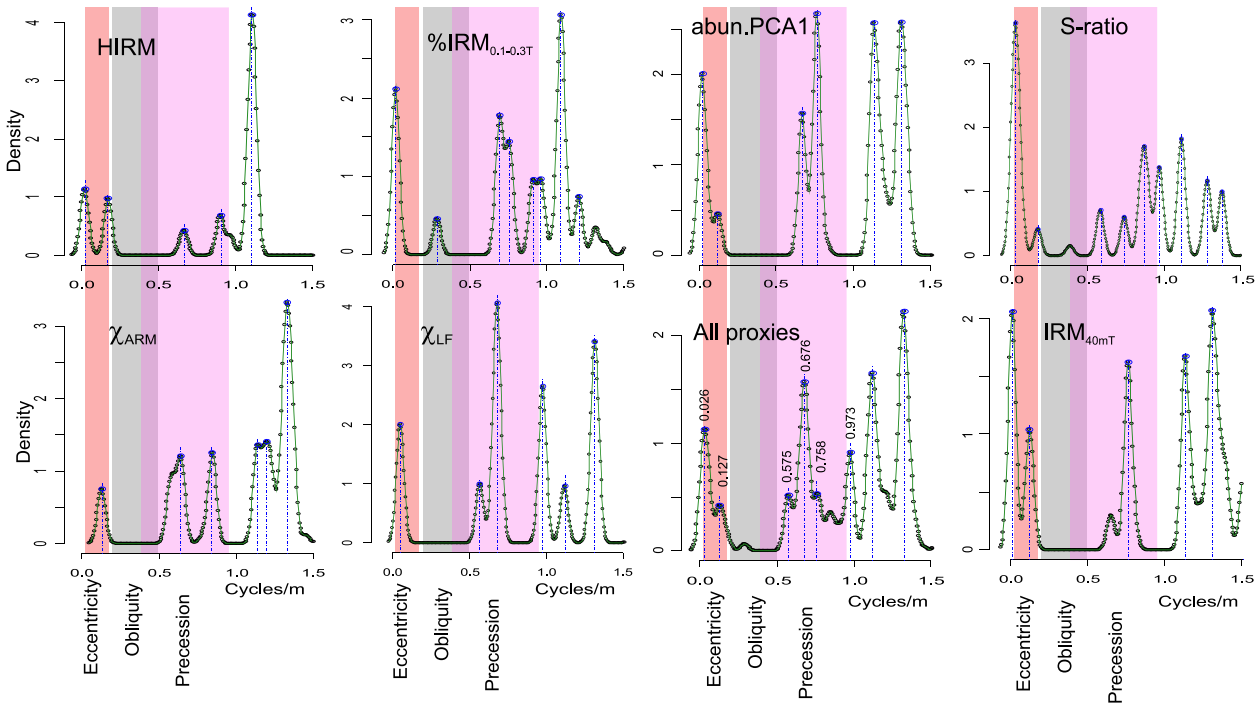

Figure 8. Kernel density estimates of the distribution of significant frequencies with frequency (probability, ≤0.05), using the LOWSPEC method. This data includes multiple peaks for the range of interpolated sample spacings. Kernel density uses 0.025 cycles/m bandwidth. The colored bands indicate the likely range of astronomical periods based on the likely range in SAR detailed in the text (which is 6–12 cm/kyr). Only those peaks with <1 cycles/m are considered important here, using the cut-off criteria of Kemp (2016). All proxies data are the agglomerated peaks from all the proxies and all the tested interpolation intervals, with the peak frequencies indicated.

5. Results: Astrochronologic Testing

5.1. Nominal Constant Sediment Accumulation Rates

Spectral analysis of the peak positions using the kernel density estimates of the LOWSPEC peaks (based on the multiple-tests of interpolation interval) are somewhat variable between the magnetic proxies (Figure 8). Using the above radioisotopic-derived average SAR estimates, the proxies clearly display frequencies largely in the eccentricity and precession frequency bands (Figure 8), with only minor obliquity-band peaks, which are more evident with the $\%IRM_{0.1–0.3T}$ parameter. Agglomeration of the selected peak positions produces an overall summary (all-proxies) from all of the data sets in this procedure (Figure 8). Overall, the data largely display 1–2 peaks in the eccentricity band, and 2–3 in the precession band. If the first five spectral peaks in the all proxies set are E1, E2-3, P1, P2, P3-4, then the average SAR using the astronomical periods for the Asbian (from Table S1 in Supporting Information S1) are 9.5, 7.1, 8.3, 7.3, 7.6 cm/kyr, respectively. These are within the SAR window range expected, based on the arguments made in Section 4.4.

The average spectral misfit (ASM) test of the accepted peaks, shows that the lowest ASM, and optimum null-hypothesis significance levels (H_o-SL <1%) are shown by S-ratio, χ_{ARM}, all-proxies and abun.PCA1 (Figure 9c). These three optimum proxies suggest the average SAR is around 5.5–7.5 cm/kyr (Figures 9a and 9b). These are within the SAR range anticipated, from Section 4.4, and suggest that the magnetic proxies are reflecting astronomically driven forcing, with some rather better than others, if the H_o-SL is a guide (Figure 9c). The ASM-derived average SAR is a closer match to the Belgium-derived Asbian duration estimates with its uncertainty interval of 5.0–7.7 cm/kyr. However, the inconsistency in the optimum SAR from the ASM analysis is probably related to a variable SAR in the section, and a variable response of the proxies to climatic forcing.

Variable SAR will more severely distort any precession and obliquity scale forcing, than that of eccentricity, which instead should provide a more reliable expression of likely astronomically driven forcing (Meyers, 2019). An alternative approach to using spectral analysis and ASM is to evaluate the nominal constant SAR model using TimeOpt, and short eccentricity modulation. This by-passes the need for spectral peak estimates like used in the ASM. Analysis using TimeOpt indicates two dominant modes in the SAR, between ~5.5 and 10 cm/kyr with the

25724525, 2024, 3, Downloaded from https://agupubs.onlinelibrary.wiley.com/doi/10.1029/2023PA004772 by Spanish Cochrane National Provision (Ministerio de Sanidad), Wiley Online Library on [02/04/2024]. See the Terms and Conditions (https://onlinelibrary.wiley.com/terms-and-conditions) on Wiley Online Library for rules of use; OA articles are governed by the applicable Creative Commons License

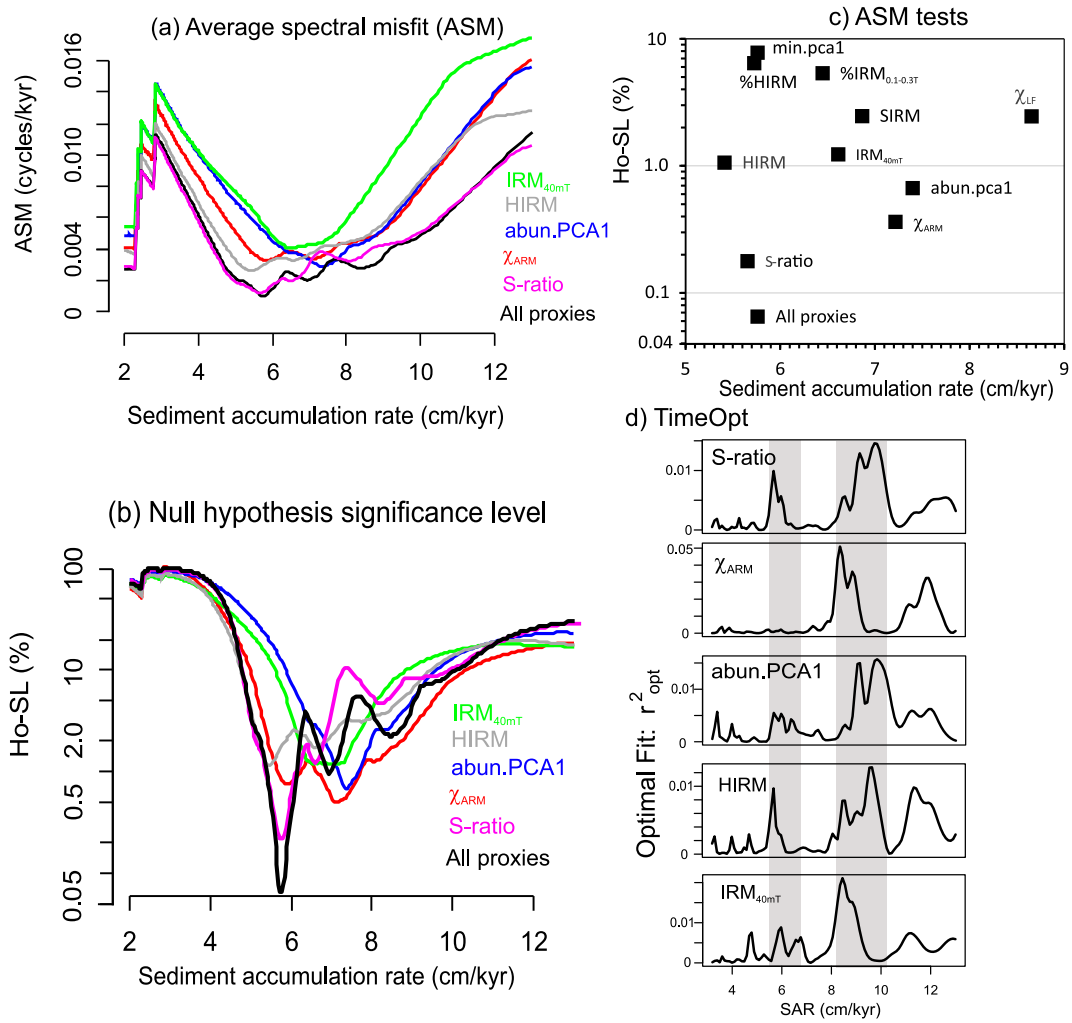

Figure 9. Data from the average spectral misfit (ASM) analysis and nominal TimeOpt sedimentation accumulation rate (SAR) assessment. (a) the ASM values with SAR for the proxies with null hypothesis significance level (Ho-SL) less than 2% and (b) the corresponding significance level of these with SAR. (c) All the variables tested and their peak significance level and corresponding SAR. (d) Variation of optimal eccentricity modulation fits (r^2_{opt}) using TimeOpt on those variables from ASM with the smaller %Ho-SL. Spectral peaks used are those in Figure 8 and with astronomical periods in Table S1 in Supporting Information S1. Full ASM results in Table S3 in Supporting Information S1. TimeOpt in (d) uses only eccentricity periods and short eccentricity modulation.

larger r^2_{opt} mode at ~8.3–10 cm/kyr (Figure 9d). These r^2_{opt} variations are largely driven by the envelope fits rather than the power-fits using TimeOpt. The antithetical behavior between envelope and power fits are strongly dependent upon the character of the noise (Meyers, 2015). Indeed, the estimated ρ_{AR1} for S-ratio, χ_{ARM}, abun. PCA1, HIRM, and IRM_{40mT} are 0.83, 0.81, 0.78, 0.84, 0.67 respectively, indicating relatively strong red processes for these data sets (Meyers, 2012; Weedon, 2022a). In summary, using TimeOpt like the ASM analysis, suggests the two modes are a likely reflection of a variable SAR in the section, which is evaluated below.

5.2. Variable Sedimentation Rate Models for Trowbarrow

Evolutive spectral methods have proven useful for determining variable SAR in astronomically forced data sets (Meyers et al., 2001; Meyers & Sageman, 2004; Schaaf & Thurow, 1997; Zou et al., 2016). This especially focusses on those five proxies with the smaller H_o-SL from the ASM analysis, since these may provide the stronger expression of astronomical forcing and therefore may be better at determining SAR changes (i.e., S-ratio, χ_{ARM}, abun.PCA1, HIRM, and IRM_{40mT}; displayed in Figure 9). Using evolutive harmonic analysis (EHA; Meyers et al., 2001), these five best proxies show the prominence of power mostly in the eccentricity bands

25724525, 2024, 3, Downloaded from https://agupubs.onlinelibrary.wiley.com/doi/10.1029/2023PA004772 by Spanish Cochrane National Provision (Ministerio de Sanidad), Wiley Online Library on [02/04/2024]. See the Terms and Conditions (https://onlinelibrary.wiley.com/terms-and-conditions) on Wiley Online Library for rules of use; OA articles are governed by the applicable Creative Commons License

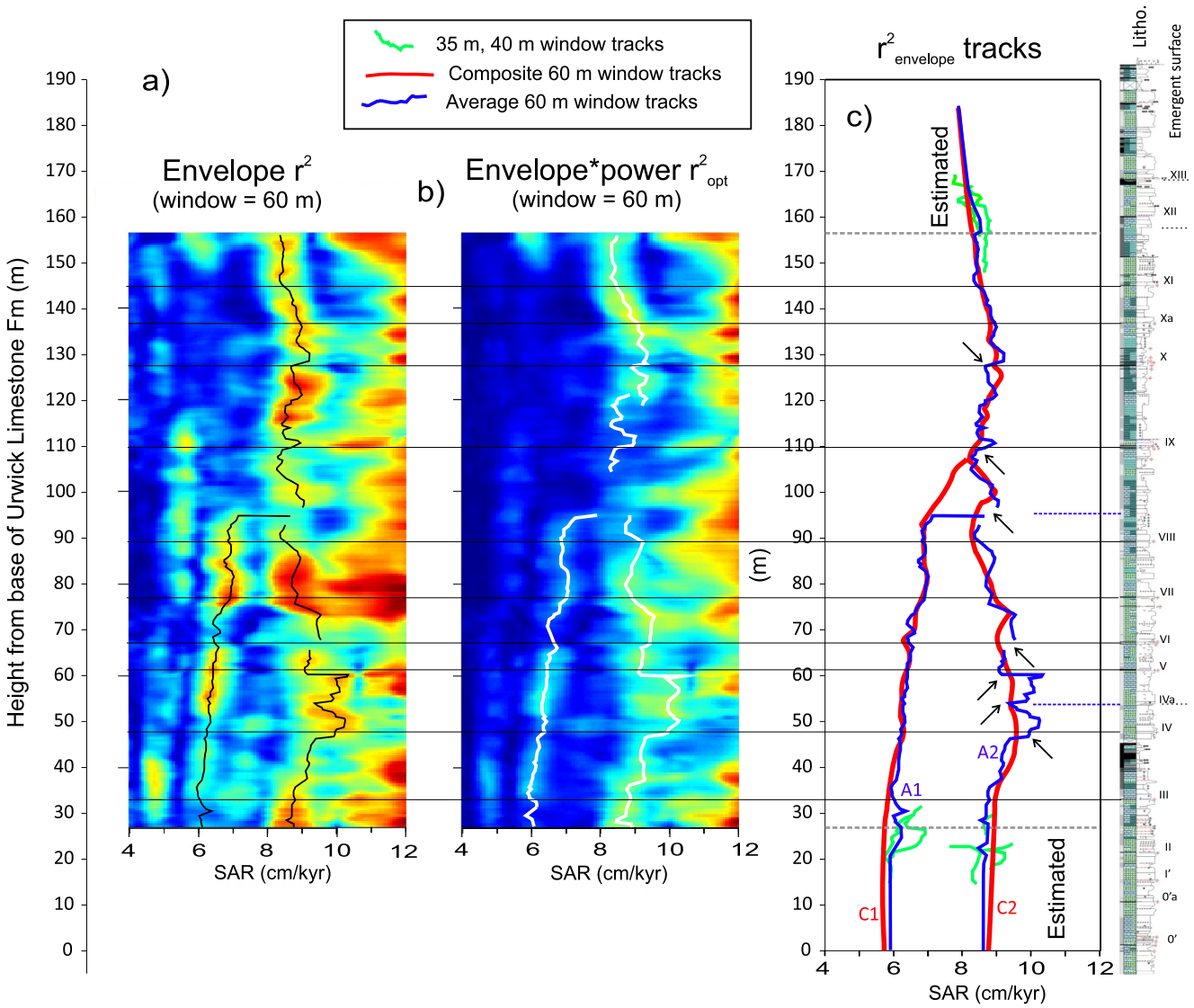

Figure 10. Averaged evolutive TimeOpt height-SAR maps with r^2 contoured with color for (a) $r^2_{envelope}$, and (b) r^2_{opt}. Red colors show largest r^2, dark blue the lowest. Shown on the maps are the inferred average SAR tracks (A1 and A2) as black and white lines. The envelope tracks are shown in (c) laid against the composite SAR tracks for the C1 and C2 SAR models (see Figures S7 and S8 in Supporting Information S1 for the individual proxy tracks) and the eTimeOpt height-SAR maps. Emergent surfaces (black horizontal line) are marked for reference points. The evolutive method cannot determine the border region at top and bottom, the width of which is dependent on the height window (60 m in this case). Interpolation interval 0.24 m, Taner roll-off = 10^{16}, short eccentricity amplitude modulation. Maps use data from χ_{ARM}, IRM_{40mT}, HIRM, S-ratio, abun.PCA1 (larger Ho-SL in Figure 9c).

throughout the section (Figure S6 in Supporting Information S1). In contrast to the LOWSPEC thresholds the EHA locally shows power in the obliquity band particularly in the magnetite abundance proxies χ_{ARM}, IRM_{40mT} and abun.PCA1 (Figure S6 in Supporting Information S1).

Any SAR to stratigraphic height model should also satisfy possible astronomical forcing in all the suitable proxies. Hence, we obtain estimates of the likely SAR-tracks from the five better proxies using two types of compilations:

1. The evolutive TimeOpt (eTimeOpt) produces a map of the r^2 values with respect to SAR and stratigraphic height (i.e., an SAR-height map). An average SAR-height map was produced by averaging the r^2 values from the SAR-height maps of the five proxies (shown in Figures 10a and 10b) for the r^2envelope and r^2opt values (individual maps are Figure S7 in Supporting Information S1). From the averaged r^2envelope SAR-height map two probable SAR tracks labeled A1 and A2 were determined. These are consistent with the radioisotopic-derived average SAR window from Section 4.4 (Figure 10c).

25724525, 2024, 3, Downloaded from https://agupubs.onlinelibrary.wiley.com/doi/10.1029/2023PA004772 by Spanish Cochrane National Provision (Ministerio de Sanidad), Wiley Online Library on [02/04/2024]. See the Terms and Conditions (https://onlinelibrary.wiley.com/terms-and-conditions) on Wiley Online Library for rules of use; OA articles are governed by the applicable Creative Commons License

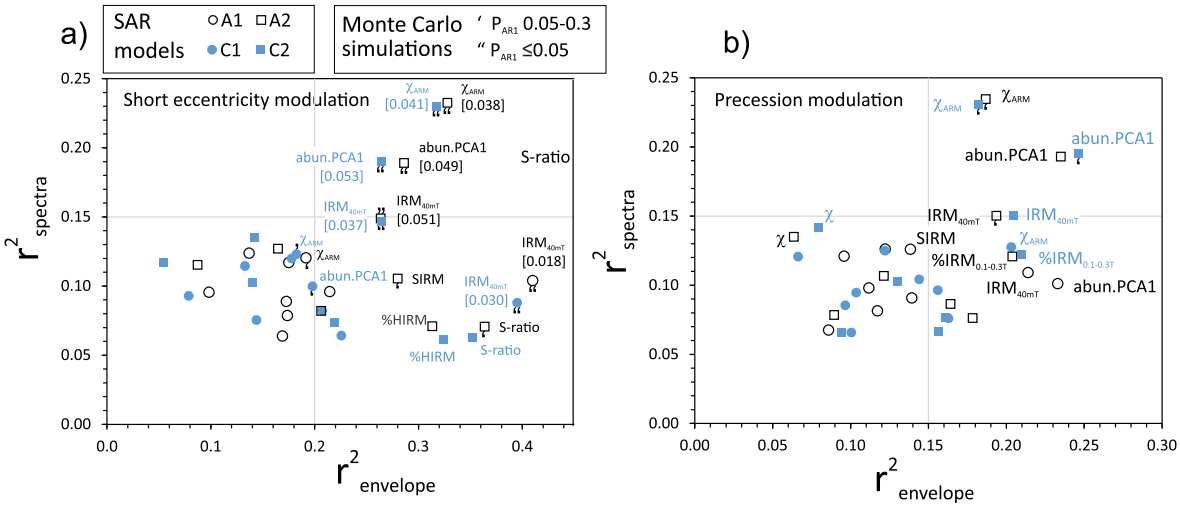

Figure 11. TimeOpt r^2 values for the four tested variable SAR models, and the cases for (a) short eccentricity modulation, and (b) precession modulation by short eccentricity (Meyers, 2015). The ticks "and" on the bases of some of the symbols indicate the null-hypothesis probability ($P_{AR1,}$ with values inside []) that the data may come from a lag 1 autoregressive (AR1) process with the same σ_{AR1} as the magnetic variable. Those with $P_{AR1} \leq 0.05$ are considered the stronger in expressing possible Milankovitch periodicities. Those not flagged have $P_{AR1} > 0.3$. The full set of data proxies shown in Figure 9c are displayed here (those not labeled).

2. Using eTimeOpt individually on the five proxies and the r^2envelope SAR-height map. The SAR tracks from the individual proxies were overlaid and visually combined to produce two likely tracks labeled as C1 and C2 shown in Figure 10c (individual SAR tracks shown Figures S7 and S8 in Supporting Information S1).

eTimeOpt used short eccentricity modulation and the eccentricity periods in Table S1 in Supporting Information S1, and in each case the SAR tracks were estimated using the SAR—height maps for $r^2_{envelope}$. The equivalent to the averaged r^2_{opt} tracks are shown for comparison in Figure 10b, but to a large extent reflects those of the $r^2_{envelope}$ map which show better defined, more continuous tracks.

The composite SAR tracks (C1, C2) are smoothed in comparison to the averaged SAR tracks due to the more variable position of the $r^2_{envelope}$ track in the averaged eTimeOpt SAR-height map (Figure 10a). SAR changes in the A2 track show some possible variability related to emergent surfaces in the section (arrows in Figure 10c). Tracks A1 and C1 join the A2 and C2 tracks between emergent surfaces VIII and IX, with the A1 and A2 tracks joining in an interval of wackestone-packstone at around a minor burrowed and reddened surface. The SAR was estimated outside the eTimeOpt maps by projecting the tracks using the 60 m window maps and the partial tracks on the averaged eTimeOpt maps for 35 and 40 m windows (top and base of Figure 10c).

Testing the suitability of the A1, A2, C1, and C2 SAR models was performed by converting the SAR to duration and using TimeOpt to test for both short eccentricity modulation and precession modulation (Figure 11). In TimeOpt the duration-scale was allowed to relax by up to ±10% to match the nearest r^2_{opt} peak in this range. These SAR "relaxations" were mostly small, for example, averaging at +2.5% and −4.7% for the A1 and A2 models. In this TimeOpt evaluation the obliquity periods (Table S1 in Supporting Information S1) were also used, hence using additional constraints to test against those used in generating the eTimeOpt derived SAR-height maps (which are based on eccentricity only). The rationale here is any suitable SAR model should additionally satisfy both obliquity and precession forcing in the data. Monte Carlo simulation was used to test the null hypothesis that an AR1 noise process (probability P_{AR1}) is different from these TimeOpt models (Meyers, 2015, 2019).

This SAR model testing demonstrates that the A2 and C2 models have the smaller P_{AR1} values (Figure 11), indicating these are the preferred SAR models. Of the proxies tested, only χ_{ARM}, IRM_{40mT}, and abun.PCA1 have P_{AR1}values which exceed the 95% confidence limit, indicating that the other proxies are not statistically distinguishable from an AR1 noise process. The A2 SAR eccentricity modulation model has a marginal advantage over the C2 model with χ_{ARM} and abun.PCA1 having smaller P_{AR1} values (Figure 11a). None of the magnetic proxies using precession modulation testing exceed a 95% P_{AR1} probability threshold, with the best being χ_{ARM}, and abun.PCA1 with a P_{AR1} of 0.18 and 0.16 respectively for the C2 SAR model, indicating some 82%–84% probability they differ from an AR1 process (Figure 11b).

25724525, 2024, 3, Downloaded from https://agupubs.onlinelibrary.wiley.com/doi/10.1029/2023PA004772 by Spanish Cochrane National Provision (Ministerio de Sanidad), Wiley Online Library on [02/04/2024]. See the Terms and Conditions (https://onlinelibrary.wiley.com/terms-and-conditions) on Wiley Online Library for rules of use; OA articles are governed by the applicable Creative Commons License

25724525, 2024, 3, Downloaded from https://agupubs.onlinelibrary.wiley.com/doi/10.1029/2023PA004772 by Spanish Cochrane National Provision (Ministerio de Sanidad), Wiley Online Library on [02/04/2024]. See the Terms and Conditions (https://onlinelibrary.wiley.com/terms-and-conditions) on Wiley Online Library for rules of use; OA articles are governed by the applicable Creative Commons License

Hence, there are marginal differences between the C2 and A2 SAR models with any precession-forcing only weakly perceptible-over the sedimentological- stratigraphic noise in the data sets. Overall, χ_{ARM} displays the slightly stronger eccentricity and precession modulation signals, with a larger r^2_{opt} and generally smallest P_{AR1} (Figure 11a). Since χ_{ARM} shows the strongest astronomical forcing, two further SAR models were tested using eTimeOpt SAR-tracks for χ_{ARM} only with the $r^2_{envelope}$ and r^2_{opt} SAR-height maps (Figure S7a in Supporting Information S1). However, using the same approach to test these, yielded no improvement in P_{AR1} or r^2_{opt} over the C2 and A2 SAR models, indicating that SAR models C2 and A2 are the most suitable.

5.3. Impact of Hiatus (or Condensed Levels)

Ascertaining the magnitude of hiatus (or condensation) at emergent surfaces from sediment characteristics is challenging, with four approaches previously used: (a) estimating the length of exposure from limestone dissolution rates using the depth of karstic pits (Walkden, 1974), (b) paleosol maturity (Vanstone, 1998), (c) erosional relief on the emergent surfaces (Horbury & Adams, 1996), and (d) under the assumption that limestone rhythms represent a ~100 kyr short eccentricity cycle, missing parts provide an estimate of hiatus (Strasser, 2016; Vanstone, 1996). These methods perhaps give some idea of relative rates, but quantitative estimates of lost or condensed time in Asbian successions are open to much uncertainty, but perhaps more robust estimates have been attempted on Cretaceous carbonate platforms (Strasser, 2016). Nevertheless, the qualitative assessment of Vanstone (1998) suggested that hiatuses at Asbian emergent surfaces may range from a few 100 years to a few 10 kyr. The estimates of Walkden (1974) range from 8 kyr to an extreme 100 ka, but overall, are of a similar order of magnitude as Vanstone (1998). Here, approach (d), is used to quantitatively estimate the mismatch of the eccentricity signal across possible hiatuses (Meyers, 2019). This uses the astrochron timeOptTemplate function and eccentricity modulation to test possible time-loss models at selected emergent surfaces using both the A2 and C2 SAR models. Practically, this loss is modeled with a low SAR at one interpolated datapoint (at 0.22 m spacing) nearest the emergent surface. TimeOptTemplate simply scales the input SAR model over a range of average SAR values searching for a maximum in r^2_{opt}. Since a precession signal is only weakly present in the Trowbarrow data set, it is likely that the resolution of this eccentricity-scale approach is limited, and hence anything less than about 10 kyr loss is likely untestable with this approach. Hence this assessment focusses on the likely major emergent surfaces.

A short-list of possible emergent surfaces with circumstantial evidence for a major hiatus was compiled based on the following criteria: (a) Intervals of disturbance in the short eccentricity fits for SAR models A2 and C2 (Figure S9 in Supporting Information S1) suggesting emergent surfaces I', II and IX; (b) Paired bifurcations in the obliquity peaks in the averaged EHA map (surfaces I' and II; Figure 12a) and also abrupt shifts in the eccentricity peaks (surfaces VI and X; Figure 12a, Figure S6 in Supporting Information S1), based on the hiatus modeling work of Meyers et al. (2001) and Meyers and Sageman (2004); (c) Major supratidal intervals in the Trowbarrow section and major clusters of minor paleosols (surfaces VI, IX, X; Figures 3b and 3e); (d) The most severely mammilated surface with the thickest paleosol at Trowbarrow (surface VII); (e) Paleovalleys known from ULF sections in the Carnforth area (7.5 km SSE of Trowbarrow) suggesting surfaces VIII (or IX) and III (from data in Horbury, 1987; detailed in Supporting Information S1).

These short-listed surfaces were tested individually using the C2 and A2 SAR models and timeOptTemplate, looking for: (a) stable hiatus solutions that achieved an improvement in r^2_{opt} over the no hiatus model (last column of Table 3); (b) gave hiatus durations greater than or equal to ~10 kyr and (b) gave solutions which approximately matched the C2 and A2 SAR models outside the hiatus level. This evaluation used the better three magnetic proxies (χ_{ARM}, IRM_{40mT}, abun.PCA1). In this approach it is assumed those surfaces consistently scoring the larger improvement in r^2_{opt} (over the no-hiatus r^2_{opt} values) are the most likely locations of major hiatus in the section. Individual testing of the emergent surface short list indicates that only surfaces II and VI are consistently selected with all three proxies and in both SAR models using this approach (Table 3). Of the remaining surfaces VII more consistently scores increases in r^2_{opt} (over the no-hiatus model) with similar hiatus amounts, than the next most likely surface which is I'. Hence, surfaces II, VI and VII were tested in modifications to the SAR models C2 and A2 (flagged in two- and three-hiatus part of Table 3), with surfaces II and VI being the primary and VII being the secondary test targets to test.

Since the individual-hiatus tests may capture partly lost cycles from other emergent surfaces; to find a solution using two (or more) hiatuses it is necessary to search the hiatus duration space for both surfaces

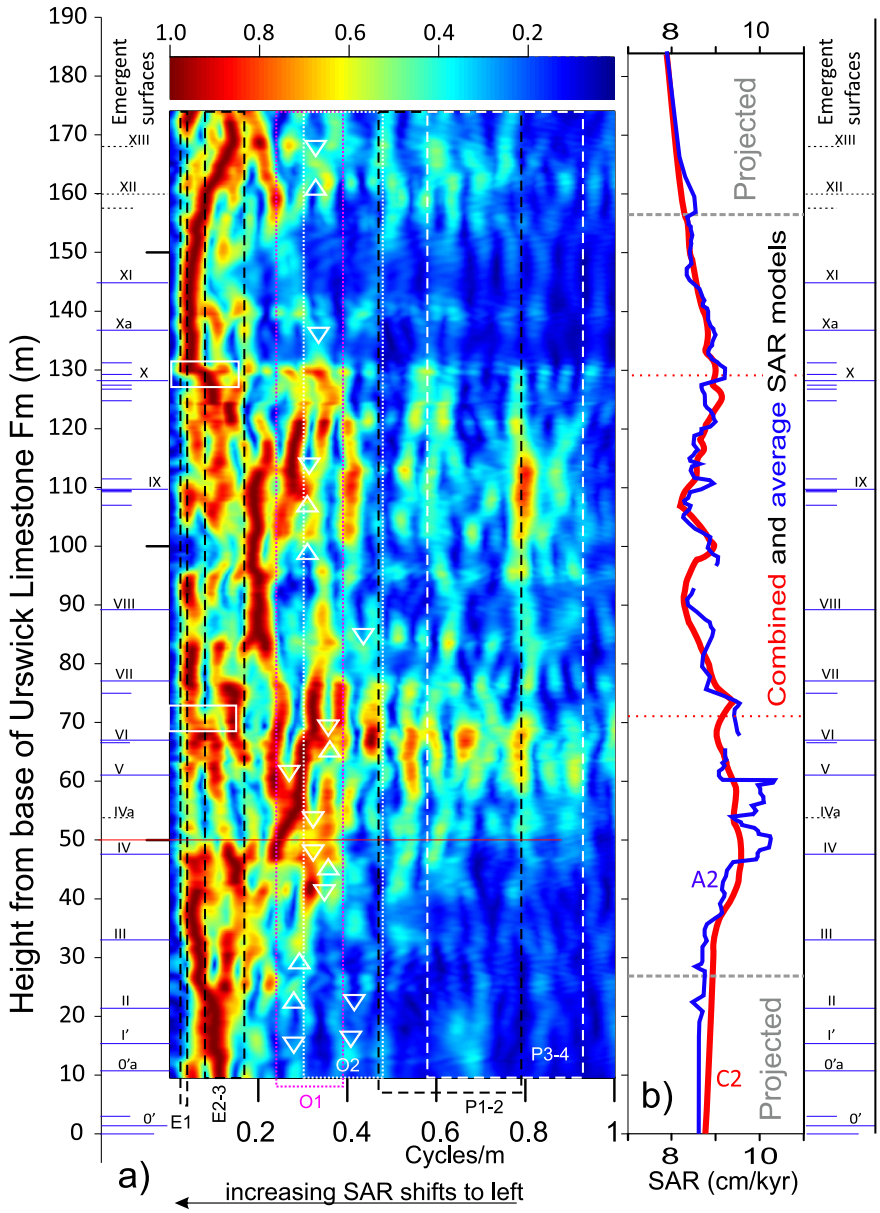

Figure 12. (a) Averaged evolutive harmonic analysis (EHA) height-amplitude map generated from the individual EHA maps for IRM40mT, χ_{ARM} and abun.PCA1 (window size = 25 m, step = 0.24 m, multi-taper time bandwidth product = 3, log of spectral power). Emergent surfaces marked as in Figure 3. The boxes with dashed lines mark the expected range of long eccentricity (E1), short eccentricity (E2-3), obliquity (O1, O2) and precession (P1-2, P3-4) using the estimated average range in accumulation rates from the radioisotopic correlations. The white triangles indicate bifurcations in obliquity-scale peaks, with triangle peak at closed end of bifurcation, and bases on bifurcated side. White boxes indicate major discontinuities in the eccentricity ridges. (b) the sedimentation accumulation rate (SAR) curves for the C2 and A2 models.

simultaneously in timeOptTemplate to find the maximum r^2_{opt} value in this 2-dimensional space. For the two-hiatus test χ_{ARM} was chosen since this shows the largest increase in r^2_{opt} for surfaces II and VI (22% and 18% improvement over the non-hiatus models in last column of Table 3) for the individual hiatus tests (Table 3). An additional constraint is that ideally this should be less than or equal to the median duration from the individual-hiatus tests, since this also satisfies the other proxies. Hence, for the two-hiatus case the limits of this space explored were between 10 kyr and the median hiatus duration (61 kyr) and 31 kyr for surfaces II and VI from the individual tests (Table 3). The results from searching this space are in Figures S10a and S10b in Supporting Information S1. The two-hiatus tests improve the r^2_{opt} over the individual hiatus tests

25724525, 2024, 3, Downloaded from https://agupubs.onlinelibrary.wiley.com/doi/10.1029/2023PA004772 by Spanish Cochrane National Provision (Ministerio de Sanidad), Wiley Online Library on [02/04/2024]. See the Terms and Conditions (https://onlinelibrary.wiley.com/terms-and-conditions) on Wiley Online Library for rules of use; OA articles are governed by the applicable Creative Commons License

25724525, 2024, 3, Downloaded from https://agupubs.onlinelibrary.wiley.com/doi/10.1029/2023PA004772 by Spanish Cochrane National Provision (Ministerio de Sanidad), Wiley Online Library on [02/04/2024]. See the Terms and Conditions (https://onlinelibrary.wiley.com/terms-and-conditions) on Wiley Online Library for rules of use; OA articles are governed by the applicable Creative Commons License

Table 3
Evaluation of Hiatus at Emergent Surfaces Using TimeOptTemplate (Fits For Short Eccentricity Modulation), For Individual Hiatuses, and the Two- and Three Hiatus Tests

			Emergent surface tested							r^2_{opt}, no
SAR model	Proxy	I'	II	III	VI	VII	VIII	IX	X	Hiatus
Individual hiatus timeOptTemplate tests										
C2	χ_{ARM}	0.074[109]	0.066[112]	0.061[87]	0.061[28]	0.059[69]	n.s	0.055[89]	n.s	0.052
C2	IRM_{40mT}	0.036[8]	0.041[17]	0.041[38]	0.049[38]	0.053[70]	0.033[22]	0.036[268]	n.s	0.039
C2	abun.PCA1	0.048[10]	0.052[16]	n.s	0.049[13]	n.s	n.s	n.s	n.s	0.045
A2	χ_{ARM}	0.071[96]	0.064[104]	0.059[81]	0.061[31]	0.061[86]	0.058[118]	0.054[92]	0.052[6]	0.053
A2	IRM_{40mT}	n.s	0.037[209]	0.037[40]	0.051[38]	0.055[72]	0.039[12]	0.035[280]	0.039[9]	0.039
A2	abun.PCA1	n.s	0.052[9]	0.048[14]	0.054[30]	0.051[11]	0.051[8]	n.s	0.050[8]	0.050
Median duration (kyr)		53	61	40	31	70	17	180	8	
							SARmin	**SARmax**	**min/max**	
Two hiatus timeOptTemplate tests										
C2	χ_{ARM}		0.081[28]		0.081[18]		0.10[221]	10.07	7.90/9.58	0.052
A2	χ_{ARM}		0.075[31]		0.075[20]		0.21[107]	10.76	7.90/10.34	0.053
Three hiatus timeOptTemplate tests										
C2	IRM_{40mT}		0.068[28]		0.068[34]	0.068[20]	0.67[33]	10.15	7.90/9.58	0.039
A2	IRM_{40mT}		0.067[31]		0.067[78]	0.067[31]	0.64[35]	10.81	7.90/10.34	0.039

Note. In each case the number is r^2_{opt}, followed by effective hiatus duration (in kyr) inside [] as determined by timeOptTemplate. The two-hiatus tests found the maximum r^2_{opt} in the 2-D space between 10 kyr and the median of the respective hiatus in each, which were 61 and 31 kyr for surfaces II and VI respectively. The three-hiatus tests used a fixed hiatus for surface II from the two hiatus test. Ones in gray text do not or barely exceed the r^2_{opt} for the no hiatus models. Ones flagged in yellow exceed the no-hiatus r^2_{opt} by the largest amounts. N.s = none suitable either because the introduced hiatus was much less than 10 kyr, or the modeled hiatus from timeOptTemplate was not stable to changes in the input hiatus SAR or the estimated model poorly matched the input SAR model. For the two- and three hiatus tests the minimum and maximum (SARmin, SARmax) of the SAR modeled by timeOptTemplate are shown along with its modeled effective duration. For these the emergent surfaces effective durations are the input hiatuses giving the maximum r^2_{opt}.The min/max are the minimum and maximum SAR of the C2 and A2 models without hiatus. These tests used both eccentricity and obliquity targets (Table S1 in Supporting Information S1) and optimization using modulation*power. timeOptTemplate settings of difmin = 0.01, difmax = 12 and sedmin = 7.3 and sedmax = 10 were generally used and 0.22 m interpolation interval was used throughout.

(Table 3), showing this approach works, but it over-estimates the maximum hiatus (i.e., SARmin values, 221 and 107 kyr with the C2 and A2 models) compared to the smaller constrained optimum input hiatus values for II and VI (i.e., ~30 and ~19 kyr for II and VI; Table 3).

Using this simultaneous approach for three surfaces (a 3-D space) is unfeasibly expensive in run-time of timeOptTemplate, so for the three-hiatus case, surface II was fixed at the hiatus solution for the two-hiatus case (i.e., 28 and 31 kyr for SAR models C2 and A2; Table 3), and the 2-D hiatus space was similarly explored for surfaces VI and VII (Figures S10c and S10d in Supporting Information S1). Also, surfaces VI and VII are adjacent so will likely interact more strongly in the competition to satisfy parts of missing eccentricity cycles, so are the better combination to use here. To triangulate to a combined SAR model, IRM_{40mT} was used for the three-hiatus test, since this proxy shows the largest average increase (at 22% compared to no-hiatus case) in r^2_{opt} when using surface VII for the one-hiatus tests (Table 3). The three-hiatus test increases r^2_{opt} by 74% over the no-hiatus test. These three hiatus intervals are now added to the two SAR-models (A2 and C2) to generate a final astrochronology for the section (SAR models A2-3H and C2-3H). The hiatus values for surfaces II and VII were taken from the two- and three-hiatus tests respectively, and that for surface VI from the average hiatus of the two- and three-hiatus tests (49 ka, a composite solution for the χ_{ARM} and IRM_{40mT} proxies). Using the three proxies χARM, IRM_{40mT} and abun.PCA1 and these two final SAR models the P_{AR1} are all significantly different from an AR1 process (Table S5a in Supporting Information S1).

5.4. A Duration for the Late Asbian

With the advantage of several likely astronomically forced proxies and two likely age models, the approach used is to generate a combined estimate of the late Asbian duration, with uncertainty. This is different to

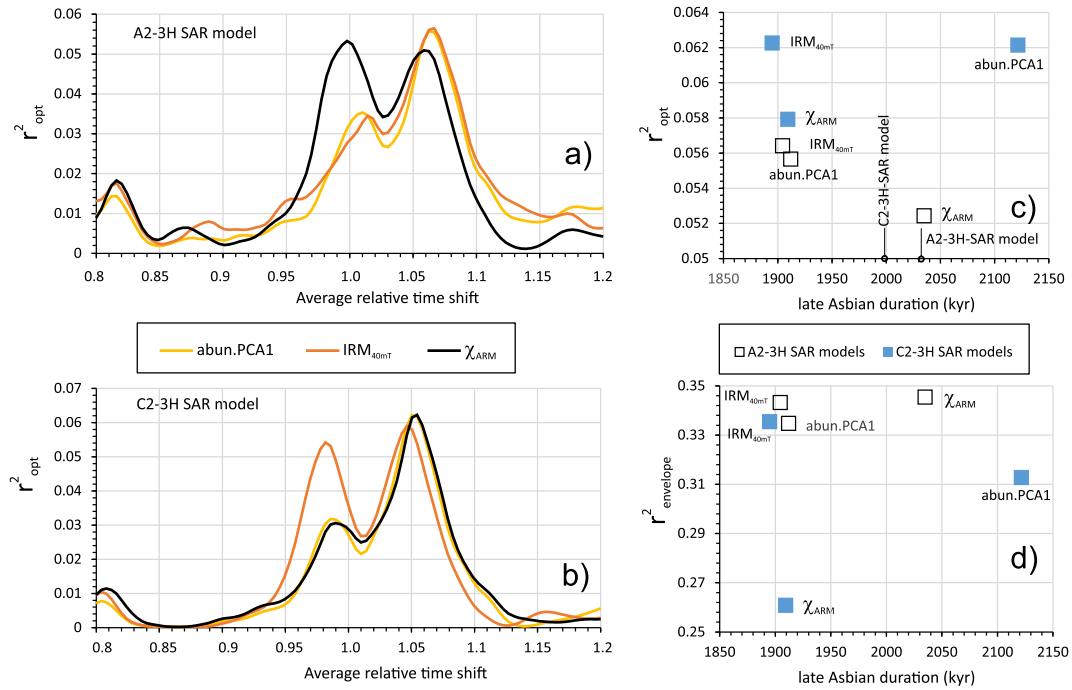

Figure 13. Output from TimeOpt for the three hiatus models for; (a) the A2-3H SAR model and (b) the C2-3H SAR model. In each case the three best proxies used to train the three hiatus runs are shown. Relative time shift is the proportional linear change in the time axis, so 1.05 would be an average 5% increase of duration. (c) and (d) are the r^2_{opt} and $r^2_{enveope}$ values for the six cases shown in (a) and (b) against the duration of the late Asbian from TimeOpt.

classical tuning approaches which tend to consider one spectral peak for tuning (e.g., Weedon, 2022b), and select the best (largest r^2_{opt}) of these predictors (e.g., χ_{ARM} with the C2 SAR model and two hiatuses; Table 3). However, our approach conforms with multiple astrochonologic testing approaches now more widely being applied to some data sets (Da Silva et al., 2020). Like the prior tests of the variable sedimentation rate models A2 and C2, the final astrochronology uses the A2-3H and C2-3H SAR models and converts the SAR to duration and uses TimeOpt with short eccentricity modulation for the final time-models. These TimeOpt solutions select the largest r^2_{opt} peak and give small relaxations of the time axis between 0% and +7% (Figures 13a and 13b). The details of the TimeOpt evaluations of these two SAR models with the three hiatuses are shown in Table S4 in Supporting Information S1 (for both eccentricity and precession modulation).

The duration of the late Asbian varies a little between the estimation proxies (Figure 13c). Also, the C2-3H SAR models give overall larger r^2_{opt}, but the A2-3H models give larger $r^2_{envelope}$ values (Figure 13d). An overly optimistic estimate of the late Asbian duration using only the four models clustered close to 1,900 kyr suggests an average duration of 1905 ± 8 kyr (1σ). A probably more realistic estimate of the late Asbian duration is 1976 ± 86 kyr (1σ), which uses all six sets of proxies and SAR models and the two SAR age models, since these were derived from the evolutive methods and were improved by adding the timeOptTemplate derived hiatuses (Figure 13d). Although the precession modulations give a lower r^2_{opt} than the eccentricity modulation, the section time durations from the three better proxies are comparable between the eccentricity and precession modulations fits from TimeOpt (Table S4 in Supporting Information S1).

Currently, the best estimate to anchor this floating astrochronology is to link it to the approximate base Brigantian age from radioisotopic date W13 at 332.5 ± 0.18 Ma from the Belgium sections, which would give the base of the late Asbian as 334.48 ± 0.35 Ma (2σ), using the realistic estimate of duration.

6. Discussion

It is likely that there are SAR changes at the scale of the carbonate rhythms and magnetic cycles in the section (shown in Figures 3 and 4). The evolutive methods inevitably average these out because of the wide-height

25724525, 2024, 3, Downloaded from https://agupubs.onlinelibrary.wiley.com/doi/10.1029/2023PA004772 by Spanish Cochrane National Provision (Ministerio de Sanidad), Wiley Online Library on [02/04/2024]. See the Terms and Conditions (https://onlinelibrary.wiley.com/terms-and-conditions) on Wiley Online Library for rules of use; OA articles are governed by the applicable Creative Commons License

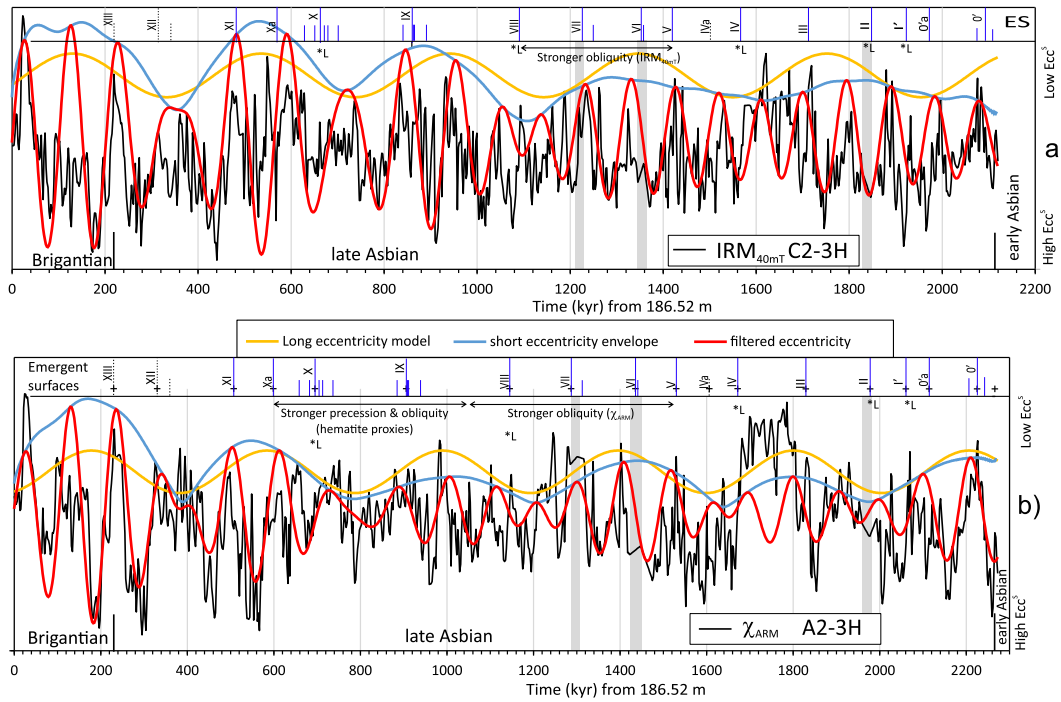

Figure 14. Summary age models for the three-hiatus SAR models C2 and A2 showing the long and short eccentricity models and the filtered eccentricity model to the data (Taner filter roll-off = 10^{16}, interpolated spacing in time of 2.2 kyr). (a) That for IRM_{40mT} uses the C2-3H model (with $r^2_{opt} = 0.063$ as in Figure 13c), and that in (b) uses χ_{ARM} and the A2-3H model (with $r^2_{opt} = 0.052$ as Figure 13d). The emergent surfaces (ES) are marked as in Figure 3, and the position of the modeled hiatus levels shown as gray vertical bars. High and low Ecc^S are the direction of high and low short eccentricity, when the fitted eccentricity cycles are phased to climate model predictions. *L = emergent surface approximately coincident with high Ecc^S.

window needed to extract a stable SAR track. To extract a locally more variable SAR at the scale of the rhythms and cycles, geochemical proxies would likely be needed for productivity or stasis in the section, in order to provide a better SAR proxy. These could then be added to the longer-term SAR changes to test against astro-chronologic models based on the timeOptTemplate method. This kind of approach would likely yield better precession-scale fits than obtained here. The alternative is to study in the same way as here, several other sections which cover the same stratigraphic interval, which, if combined, would yield a more robust estimate of the late Asbian and inter-hiatus durations. The additional sections and cores examined by Cózar, Somerville, Hounslow, and Coronado (2022) from elsewhere in Britain and Ireland would be suitable future targets for this interval.

Eccentricity-paced climate change driven by polar ice volumes has long been inferred as the key pacer of mid and late Carboniferous climate change. Glacio-eustatic changes in sea-level as expressed in the emergent surfaces in the Trowbarrow succession are one component of that change. The positioning of emergent surfaces indicates a general correspondence with peaks in short eccentricity cycles (surfaces O', O'a, III, V, VII, IX, XI; Figure 14). Surface XIII also has a good correspondence but is not an emergent surface in Trowbarrow, but a rhythm-top (Cózar, Somerville, Hounslow, & Coronado, 2022). However, surfaces I', II, IV, VIII and possibly X show better correspondence to lows in short eccentricity. These latter cases are to a large extent coincident with lows in long-eccentricity (Figure 14), and the former cases with highs in long eccentricity. However, since sea-level changes are likely driven by polar ice volume fluctuations, and the changes in clastic supply (expressed by the magnetic proxies), are a low-latitude climate and paleoceanographic response, expectations of a wholesale one-to-one coincidence in peaks in short eccentricity and hiatus positions are unrealistic.

How these eccentricity changes are phased to actual astronomical targets cannot be ascertained from the data alone. The astronomically driven climate model for the Late Paleozoic of Horton et al. (2012) suggests the maximum high-latitude ice storage and lows in sea-level occurred during synchronized lows in short eccentricity and obliquity, corresponding to the maximum draw-down in sea-level. This eccentricity response is opposite to the Trowbarrow data sets, suggesting that the observed eccentricity modulations are anti-phased with the real

25724525, 2024, 3, Downloaded from https://agupubs.onlinelibrary.wiley.com/doi/10.1029/2023PA004772 by Spanish Cochrane National Provision (Ministerio de Sanidad), Wiley Online Library on [02/04/2024]. See the Terms and Conditions (https://onlinelibrary.wiley.com/terms-and-conditions) on Wiley Online Library for rules of use; OA articles are governed by the applicable Creative Commons License

peaks in short eccentricity. Using this calibration to the climate model predictions, the properly phased short eccentricity cycles are referred to as low and high Ecc^S (Figure 14) to distinguish them from the fitted cycles. More detailed climate modeling work for the late Paleozoic (Heavens et al., 2015) generally concurs with that of Horton et al. (2012). It suggests that low paleolatitude monsoonal-dominated successions in Pangea should show strong variability at both eccentricity and precession frequencies, primarily driven by changes in atmospheric greenhouse gases and sea-level driven by changes in ice volume. The statistical significance of any modulated precession signal at Trowbarrow is somewhat lower than that of eccentricity modulation, with χ_{ARM} and IRM_{40mT} showing the smaller P_{AR1} (Table S5b in Supporting Information S1). In contrast, the EHA data suggests precession is locally most strongly expressed in the hematite-proxy data (S-ratio, HIRM; Figure S6 in Supporting Information S1) in the interval between surfaces VIII and Xa (arrow on Figure 14b), in spite of poorer overall fits (Tables S4b and S4d in Supporting Information S1).

The eccentricity cycles are best expressed by the magnetite and marine-clastic-based proxies χ_{ARM}, IRM_{40mT}, and abun.PCA1, which also show a strong connection with the carbonate-rhythms in the section. If the eccentricity phasing linked to the model of Horton et al. (2012) is correct, the observed peaks in clastic supply relate most strongly to lows in Ecc^S. This may also be the case for long eccentricity, which combines to produce stronger expression in the highs in magnetite-abundance (e.g., interval younger than emergent surface X; Figure 14).

The overlying Brigantian in the region of the SCS sees the start of the limestone-shale-sandstone cyclothems which typically characterize the Serpukhovian and Pennsylvanian in northern England (Tucker et al., 2009). The data from Trowbarrow captures the initial start of this change (Figure 14). The essentially clastic-content related magnetite-based cycles seen in the ULF can therefore be inferred to be an older and much-muted expression of the clastic supply driven cyclothems which characterize younger Carboniferous strata (Fielding, 2021). Indeed, in NW Cumbria the late Asbian succession shows shale units interbedded with limestones, showing a similar number of depositional cycles as the ULF (Thurlow, 1996), although any detailed correlation is currently unclear without a high-resolution biostratigraphy for the NW Cumbrian Asbian. The catchments supplying material to the Cumbrian Asbian successions were probably quite small, so siliciclastics were largely retained in the northern part of the ramp (Figure 1a; Wakefield et al., 2016).

Sediment supply in equatorial regions with seasonal climates is reasonably well understood, and is strongly related to precipitation, catchment relief and vegetation, with larger riverine loads in monsoonal and more storm-prone catchments (Van der Zwan, 2002). By analogy, in the Neogene, the Niger River in equatorial west Africa showed largest sediment yields during dry seasons which were intensified by short eccentricity cyclicity, producing a strong enhancement in supplied loads (Van der Zwan, 2002). In equatorial Pangea, in the late Paleozoic, climate modeling suggests that the climate was dryer when ice sheets were bigger compared to times of diminished ice sheets (Heavens et al., 2015). These connections suggest a model of larger sediment yields during late Asbian lows in sea-level (i.e., either side of the lowstand represented by the emergent surface), which is what is seen in the Trowbarrow data set. The drier climate close to lowstands also tallies with the enhanced eolian supply of hematite-rich siliciclastics which characterize the regressive parts of the carbonate rhythms and the terrestrially derived paleosols (Figures 3 and 6). Oplustil et al. (2022) have proposed a similar environmental model for early Pennsylvanian paralic clastics, but implicated stronger seasonality driving enhanced clastic loads, via lesser vegetation cover around sea-level low stands.

Naturally, any siliciclastic supply needs to be distributed across the carbonate ramp. One mechanism which could enhance distribution of siliciclastic supply during low Ecc^S is proximity to the progradation of siliciclastics from the north coincident with the lowering of sea-levels prior to the lowstand. Wave and tide action would disperse the finer-clastics across the ramp during the shallowing regressive phase. The siliciclastics stored on the ramp may then be reworked during the following transgressive phase associated with increasing Ecc^S. This scenario is broadly like that inferred on the Great Barrier Reef during Quaternary low stands, with trapping of siliciclastics on the shelf-top by topographic highs and lows and subsequent redistribution during marine transgression (Dunbar et al., 2000; Thran et al., 2020). There is some evidence for siliciclastic-trapping in NW Cumbria Asbian successions, where variable limestone-clastic compaction has resulted in thickness variations, as near-shore clastics prograded over more distal carbonates (Thurlow, 1996). The alternative "reciprocal sedimentation model" of Wilson (1967) in which the siliciclastics by-pass the ramp at low stands via channels is probably not appropriate for the SCS ramp, since whilst low-stand channels on the ramp front are known from the Carnforth area (Horbury, 1987), they are not known from elsewhere in the ULF.

25724525, 2024, 3, Downloaded from https://agupubs.onlinelibrary.wiley.com/doi/10.1029/2023PA004772 by Spanish Cochrane National Provision (Ministerio de Sanidad), Wiley Online Library on [02/04/2024]. See the Terms and Conditions (https://onlinelibrary.wiley.com/terms-and-conditions) on Wiley Online Library for rules of use; OA articles are governed by the applicable Creative Commons License

25724525, 2024, 3, Downloaded from https://agupubs.onlinelibrary.wiley.com/doi/10.1029/2023PA004772 by Spanish Cochrane National Provision (Ministerio de Sanidad), Wiley Online Library on [02/04/2024]. See the Terms and Conditions (https://onlinelibrary.wiley.com/terms-and-conditions) on Wiley Online Library for rules of use; OA articles are governed by the applicable Creative Commons License

7. Conclusions

Rock magnetic data from the Trowbarrow section show cyclical changes, which are linked to both the carbonate rhythms and emergent surfaces in the section. Rock magnetic changes are principally related to two kinds of clastic sources. Firstly, a magnetite-dominated source, particularly expressed by χ_{ARM} and IRM_{40mT} which are linked to the shaley and more argillaceous intervals in the section. Secondly, to a hematite-dominated source expressed by S-ratio and HIRM, linked to eolian input spatially connected with regressive intervals underlying the emergent surfaces, and paleosols in the section. An environmental model is proposed that links changes in clastic-sources and magnetic proxies to the carbonate-based rhythms.

The average spectral misfit suggests the magnetic proxies S-ratio, abun.PCA1, $\chi_{ARM,}$ HIRM, and IRM_{40mT} show the stronger evidence of Milankovitch-forcing, with probabilities exceeding the 98% significance level. Sedimentation rate models for the section utilized these better five proxies as guides in evolutive analysis. Optimum SAR models used two differing approaches generating two viable SAR models, based on constraints of average SAR from correlated radioisotopic dates for the Asbian. When tested with TimeOpt methods (using eccentricity modulation), using the five magnetic proxies, the two SAR models are equally probable, and largely differ only in the regularity of the SAR changes. The proxies which better express the eccentricity signals are magnetite abundance proxies χ_{ARM}, IRM_{40mT} and abun.PCA1. These three exceed the 95% significance threshold for Monte Carlo tests of a comparable AR1 process.

Hiatus at emergent surfaces in the section was tested with timeOptTemplate methods for the two SAR models using a short-list of possible significant hiatus levels. Of those hiatuses tested, three emergent surfaces were found to display the stronger evidence, based on their collective tests (and improved r^2_{opt} compared to the no-hiatus models) against the three best magnetic mineral abundance proxies. These three hiatuses were included in the two final SAR models. Based on the two final SAR models and the three better proxies, the late Asbian duration is 1976 ± 86 kyr (1σ), which can be anchored to the approximate base Brigantian radioisotopic date of 332.5 ± 0.18 Ma.

By comparison to coupled ocean-atmosphere climate models, we invert the observed amplitude of the fitted short eccentricity, such that emergent surfaces generally correspond with lows in short eccentricity. This re-phasing indicates highs in magnetite abundance proxies are related to glacio-eustatic lows in sea-level via a sediment delivery mechanism linked to increased terrestrial aridity during glacials. This conforms with the increased eolian delivery of the hematite-dominated clastic source which is enhanced during the regressive phase of the carbonate rhythms and at emergent surfaces.

Data Availability Statement

The rock magnetic data used for the cyclostratigraphic study, both the original and transformed in the study as well as the R-scripts used are available at the Figshare data repository (Hounslow et al., 2023).

Acknowledgments
MWH and AB were in part funded by NERC (Grant NE/P00170X/1) and the Leverhulme Trust (RLA-2016-080). Vassil Karloukovski, David Mindham and Courtney Sprain helped collect samples. David Mindham, Tereza Kamenikova, Vassil Karloukovski, and Elliot Hurst prepared samples and measured much of the data. Natural England, the Arnside Silverdale AONB and Lancaster City Council, allowed access, permission and permits to collect samples from the section. Comments from two anonymous reviewers improved the work.

References

Adams, A. E., Horbury, A. D., & Abdel Aziz, A. A. (1990). Controls on Dinantian sedimentation in south Cumbria and surrounding areas of northwest England. *Proceedings of the Geologists' Association*, *101*(1), 19–30. https://doi.org/10.1016/s0016-7878(08)80203-9

Burnett, R. D. (1987). Regional maturation patterns for late Visean (Carboniferous, Dinantian) rocks of northern England based on mapping of conodont colour. *Irish Journal of Earth Sciences*, *8*, 165–185.

Cózar, P., & Somerville, I. D. (2005). Stratigraphy of upper Viséan rocks in the Carlow area, southeast Ireland. *Geological Journal*, *40*(1), 35–64. https://doi.org/10.1002/gj.984

Cózar, P., Somerville, I. D., & Hounslow, M. W. (2021). Foraminifers in the Holkerian stratotype, regional substage in Britain: Key taxa for the Viséan subdivision. *Newsletters on Stratigraphy*, *55*(2), 159–172. https://doi.org/10.1127/nos/2021/0674

Cózar, P., Somerville, I. D., Hounslow, M. W., & Coronado, I. (2022). Far-field correlation of palaeokarstic surfaces in Mississippian successions using high-frequency foraminiferal diversity trends. *Palaeogeography, Palaeoclimatology, Palaeoecology*, *601*, 111088. https://doi.org/10.1016/j.palaeo.2022.111088

Cózar, P., Somerville, I. D., Hounslow, M. W., & Kamenikova, T. (2022). Proposal of a late Asbian (Mississippian) stratotype for England: Trowbarrow Quarry, S. Cumbria, UK. *Papers in Palaeontology*, *8*(3). https://doi.org/10.1002/spp2.1451

Da Silva, A. C., De Vleeschouwer, D., Boulvain, F., Claeys, P., Fagel, N., Humblet, M., et al. (2013). Magnetic susceptibility as a high-resolution correlation tool and as a climatic proxy in Paleozoic rocks–merits and pitfalls: Examples from the Devonian in Belgium. *Marine and Petroleum Geology*, *46*, 173–189. https://doi.org/10.1016/j.marpetgeo.2013.06.012

Da Silva, A. C., Mabille, C., & Boulvain, F. (2009). Influence of sedimentary setting on the use of magnetic susceptibility: Examples from the Devonian of Belgium. *Sedimentology*, *56*(5), 1292–1306. https://doi.org/10.1111/j.1365-3091.2008.01034.x

Da Silva, A. C., Sinnesael, M., Claeys, P., Davies, J. H., de Winter, N. J., Percival, L. M. E., et al. (2020). Anchoring the Late Devonian mass extinction in absolute time by integrating climatic controls and radio-isotopic dating. *Scientific Reports*, *10*(1), 12940. https://doi.org/10.1038/s41598-020-69097-6

Davies, J. R. (1982). *Stratigraphy, sedimentology and palaeontology of the Lower Carboniferous of Anglesey* Ph.D. Thesis. University of Keele.

Davydov, V. I., Crowley, J. L., Schmitz, M. D., & Poletaev, V. I. (2010). High-precision U-Pb zircon age calibration of the global Carboniferous time scale and Milankovitch band cyclicity in the Donets basin, eastern Ukraine. *Geochemistry, Geophysics, Geosystems*, *11*(2). https://doi.org/10.1029/2009GC002736

Davydov, V. I., Korn, D., Schmitz, M. D., Gradstein, F. M., & Hammer, O. (2012). Chapter 23-the Carboniferous period. In F. M. Gradstein, J. G. Ogg, M. D. Schmitz, & G. M. Ogg (Eds.), *The geologic time scale 2012* (pp. 603–651). Elsevier.

Doh, S. J., King, J. W., & Leinen, M. (1988). A rock-magnetic study of giant piston core LL44-GPC3 from the central North Pacific and its paleoceanographic implications. *Paleoceanography*, *3*(1), 89–111. https://doi.org/10.1029/PA003i001p00089

Dunbar, G. B., Dickens, G. R., & Carter, R. M. (2000). Sediment flux across the Great Barrier Reef Shelf to the Queensland Trough over the last 300 ky. *Sedimentary Geology*, *133*(1–2), 49–92. https://doi.org/10.1016/s0037-0738(00)00027-0

Embry, A. F., & Klovan, J. E. (1971). A Late Devonian reef tract on Northeastern Banks Island, NWT. *Bulletin of Canadian Petroleum Geology*, *19*, 730–781.

Fang, Q., Wu, H., Shen, S. Z., Fan, J., Hinnov, L. A., Yuan, D., et al. (2022). Astronomically paced climate evolution during the Late Paleozoic icehouse-to-greenhouse transition. *Global and Planetary Change*, *213*, 103822. https://doi.org/10.1016/j.gloplacha.2022.103822

Fielding, C. R. (2021). Late Palaeozoic cyclothems–A review of their stratigraphy and sedimentology. *Earth-Science Reviews*, *217*, 103612. https://doi.org/10.1016/jearscirev.2021.103612

Fielding, C. R., Frank, T. D., Birgenheier, L. P., Rygel, M. C., Jones, A. T., & Roberts, J. (2008). Stratigraphic imprint of the late Palaeozoic Ice Age in eastern Australia: A record of alternating glacial and nonglacial climate regime. *Journal of the Geological Society*, *165*(1), 129–140. https://doi.org/10.1144/0016-76492007-036

Flügel, E. (2004). Microfacies of carbonate rocks. In *Analysis, interpretation and application*. Springer Verlag.

Frank, U., & Nowaczyk, N. R. (2008). Mineral magnetic properties of artificial samples systematically mixed from haematite and magnetite. *Geophysical Journal International*, *175*(2), 449–461. https://doi.org/10.1111/j.1365-246x.2008.03821.x

Franke, C., von Dobeneck, T., Drury, M. R., Meeldijk, J. D., & Dekkers, M. J. (2007). Magnetic petrology of equatorial Atlantic sediments: Electron microscopy results and their implications for environmental magnetic interpretation. *Paleoceanography and Paleoclimatology*, *22*(4). https://doi.org/10.1029/2007PA001442

Gallagher, S. J. (1996). The stratigraphy and cyclicity of the late Dinantian platform carbonates in parts of southern and western Ireland. In P. Strogen, I. D. Somerville, & G. L. L. Jones (Eds.), *Recent advances in Lower Carboniferous geology* (Vol. 107, pp. 239–251). Geological Society, London, Special Publications.

Gallagher, S. J., MacDermot, C. V., Somerville, I. D., Pracht, M., & Sleeman, A. G. (2006). Biostratigraphy, microfacies and depositional environments of Upper Viséan limestones from the Burren region, County Clare, Ireland. *Geological Journal*, *41*(1), 61–91. https://doi.org/10.1002/gj.1033

Giles, P. S. (2009). Orbital forcing and Mississippian sea level change: Time series analysis of marine flooding events in the Viséan Windsor Group of eastern Canada and implications for Gondwana glaciation. *Bulletin of Canadian Petroleum Geology*, *57*(4), 449–471. https://doi.org/10.2113/gscpgbull.57.4.449

Gray, D. I. (1981). *Lower Carboniferous carbonate palaeoenvironments in North Wales* Ph.D. Thesis (p. 524). University of Newcastle.

Hays, J. D., Imbrie, J., & Shackleton, N. J. (1976). Variations in the Earth's Orbit: Pacemaker of the Ice Ages: For 500,000 years, major climatic changes have followed variations in obliquity and precession. *Science*, *194*(4270), 1121–1132. https://doi.org/10.1126/science.194.4270.1121

Heavens, N. G., Mahowald, N. M., Soreghan, G. S., Soreghan, M. J., & Shields, C. A. (2015). A model-based evaluation of tropical climate in Pangaea during the late Palaeozoic icehouse. *Palaeogeography, Palaeoclimatology, Palaeoecology*, *425*, 109–127. https://doi.org/10.1016/j.palaeo.2015.02.024

Heckel, P. H. (2013). Pennsylvanian stratigraphy of Northern Midcontinent Shelf and biostratigraphic correlation of cyclothems. *Stratigraphy*, *10*(1–2), 3–39. https://doi.org/10.29041/strat.10.1.02

Henrich, R., & Hüneke, H. (2011). Chapter 5-Hemipelagic advection and periplatform sedimentation. In H. Hüneke & T. Mulder (Eds.), *Deep-sea sediments, developments in sedimentology* (Vol. 63, pp. 353–396). Elsevier.

Hesse, P. P. (1997). Mineral magnetic "tracing" of aeolian dust in southwest Pacific sediments. *Palaeogeography, Palaeoclimatology, Palaeoecology*, *131*(3–4), 327–353. https://doi.org/10.1016/s0031-0182(97)00010-2

Hladil, J., Gersl, M., Strnad, L., Frana, J., Langrova, A., & Spisiak, J. (2006). Stratigraphic variation of complex impurities in platform limestones and possible significance of atmospheric dust: A study with emphasis on gamma-ray spectrometry and magnetic susceptibility outcrop logging (Eifelian-Frasnian, Moravia, Czech Republic). *International Journal of Earth Sciences*, *95*(4), 703–723. https://doi.org/10.1007/s00531-005-0052-8

Horbury, A. D. (1987). *The sedimentology of the Urswick Limestone in south Cumbria and north Lancashire* Unpublished PhD thesis. University of Manchester. (unpublished) Retrieved from https://www.proquest.com/openview/db5b3b5aabbee65c02a8d5ee0d42a27c/1?pq-origsite=gscholar&cbl=51922&diss=y

Horbury, A. D. (1989). The relative roles of tectonism and eustacy in the deposition of the Urswick Limestone in south Cumbria and north Lancashire. In R. S. Arthurton, P. Gutteridge, & S. C. Nolan (Eds.), *The role of tectonics in Devonian and Carboniferous sedimentation in the British Isles* (Vol. 6, pp. 153–169). Yorkshire Geological Society Occasional Publication.

Horbury, A. D., & Adams, A. E. (1996). Microfacies association in Asbian carbonates: An example from the Urswick Limestone Formation of the southern Lake District, northern England. In P. Strogen, I. D. Somerville, & G. L. L. Jones (Eds.), *Recent advances in Lower Carboniferous Geology* (Vol. 107, pp. 222–237). Geological Society, London, Special Publications.

Horton, D. E., Poulsen, C. J., Montañez, I. P., & DiMichele, W. A. (2012). Eccentricity-paced late Paleozoic climate change. *Palaeogeography, Palaeoclimatology, Palaeoecology*, *331*, 150–161. https://doi.org/10.1016/j.palaeo.2012.03.014

Hounslow, M. W., Cózar, P., Somerville, I. D., & Biggin, A. J. (2023). Rock magnetic dataset, accumulation rates and astrochronology age model for the Trowbarrow section [Dataset]. Figshare. https://doi.org/10.6084/m9.figshare.24161061.v2

Hounslow, M. W., Biggin, A. J., Cózar, P., Somerville, I. D., Kamenikova, T., & Sprain, C. J. (2024). A hyperactive geomagnetic field in the Late Visean (early Carboniferous), from the Late Asbian type section in northwest England, UK. *Geochemistry, Geophysics, Geosystems*.

Hounslow, M. W., & Maher, B. A. (1996). Quantitative extraction and analysis of carriers of magnetization in sediments. *Geophysical Journal International*, *124*(1), 57–74. https://doi.org/10.1111/j.1365-246x.1996.tb06352.x

Huang, H., Gao, Y., Ma, C., Jones, M. M., Zeeden, C., Ibarra, D. E., et al. (2021). Organic carbon burial is paced by a ~173-ka obliquity cycle in the middle to high latitudes. *Science Advances*, *7*(28). https://doi.org/10.1126/sciadv.abf9489

25724525, 2024, 3, Downloaded from https://agupubs.onlinelibrary.wiley.com/doi/10.1029/2023PA004772 by Spanish Cochrane National Provision (Ministerio de Sanidad), Wiley Online Library on [02/04/2024]. See the Terms and Conditions (https://onlinelibrary.wiley.com/terms-and-conditions) on Wiley Online Library for rules of use; OA articles are governed by the applicable Creative Commons License

Jiang, X. D., Zhao, X. Y., Zhao, X., Jiang, Z. X., Chou, Y. M., Zhang, T. W., et al. (2021). Quantifying contributions of magnetic inclusions within silicates to marine sediments: A dissolution approach to isolating volcanic signals for improved paleoenvironmental reconstruction. *Journal of Geophysical Research: Solid Earth*, *126*(10). https://doi.org/10.1029/2021JB022680

Johnson, E. W., Soper, N. J., & Burgess, I. C. (2001). *Geology of the country around Ulverston*. Memoir of the British Geological Survey, Sheet 48 (England and Wales). HMSO.

Kabanov, P. B., Alekseev, A. S., Gibshman, N. B., Gabdullin, R. R., & Bershov, A. V. (2016). The upper Viséan-Serpukhovian in the type area for the Serpukhovian stage (Moscow Basin, Russia): Part 1. Sequences, disconformities, and biostratigraphic summary. *Geological Journal*, *51*(2), 163–194. https://doi.org/10.1002/gj.2612

Kemp, D. B. (2016). Optimizing significance testing of astronomical forcing in cyclostratigraphy. *Paleoceanography and Paleoclimatology*, *31*(12), 1516–1531. https://doi.org/10.1002/2016PA002963

Kodama, K. P., & Hinnov, L. A. (2014). *Rock magnetic cyclostratigraphy*. John Wiley and Sons.

Korn, D., & Kaufmann, B. (2009). A high-resolution relative time scale for the Viséan Stage (Carboniferous) of the Kulm Basin (Rhenish Mountains, Germany). *Geological Journal*, *44*(3), 306–321. https://doi.org/10.1002/gj.1143

Larrasoaña, J. C., Roberts, A. P., Liu, Q., Lyons, R., Oldfield, F., Rohling, E. J., & Heslop, D. (2015). Source-to-sink magnetic properties of NE Saharan dust in Eastern Mediterranean marine sediments: Review and paleoenvironmental implications. *Frontiers in Earth Science*, *3*. https://doi.org/10.3389/feart.2015.00019

Liu, C., Vachard, D., Cózar, P., & Coronado, I. (2023). Middle to late Mississippian and early Pennsylvanian foraminiferal zonal scheme of South China—A case-study from the Youjiang Basin: Biostratigraphic and palaeobiogeographic implications. *Lethaia*, *56*, 1–23. https://doi.org/10.18261/let.56.1.6

Liu, Q., Roberts, A. P., Larrasoaña, J. C., Banerjee, S. K., Guyodo, Y., Tauxe, L., & Oldfield, F. (2012). Environmental magnetism: Principles and applications. *Reviews of Geophysics*, *50*(4). https://doi.org/10.1029/2012RG000393

Liu, Q., Roberts, A. P., Torrent, J., Horng, C. S., & Larrasoana, J. C. (2007). What do the HIRM and S-ratio really measure in environmental magnetism? *Geochemistry, Geophysics, Geosystems*, *8*(9). https://doi.org/10.1029/2007GC001717

McIntosh, J. A., Tabor, N. J., & Rosenau, N. A. (2021). Mixed-layer illite-smectite in Pennsylvanian-aged paleosols: Assessing sources of illitization in the Illinois Basin. *Minerals*, *11*(2), 108. https://doi.org/10.3390/min11020108

Meyers, S. R. (2012). Seeing red in cyclic stratigraphy: Spectral noise estimation for astrochronology. *Paleoceanography, Palaeoclimatology*, *27*(3). https://doi.org/10.1029/2012PA002307

Meyers, S. R. (2014). Astrochron: An R package for astrochronology. Retrieved from https://cran.r-project.org/package=astrochron

Meyers, S. R. (2015). The evaluation of eccentricity-related amplitude modulation and bundling in paleoclimate data: An inverse approach for astrochronologic testing and time scale optimization. *Paleoceanography, Palaeoclimatology*, *30*(12), 1625–1640. https://doi.org/10.1002/2015pa002850

Meyers, S. R. (2019). Cyclostratigraphy and the problem of astrochronologic testing. *Earth-Science Reviews*, *190*, 190–223. https://doi.org/10.1016/j.earscirev.2018.11.015

Meyers, S. R., & Malinverno, A. (2018). Proterozoic Milankovitch cycles and the history of the solar system. *Proceedings of the National Academy of Sciences of the United States of America*, *115*(25), 6363–6368. https://doi.org/10.1073/pnas.1717689115

Meyers, S. R., & Sageman, B. B. (2004). Detection, quantification, and significance of hiatuses in pelagic and hemipelagic strata. *Earth and Planetary Science Letters*, *224*(1–2), 55–72. https://doi.org/10.1016/j.epsl.2004.05.003

Meyers, S. R., & Sageman, B. B. (2007). Quantification of deep-time orbital forcing by average spectral misfit. *American Journal of Science*, *307*(5), 773–792. https://doi.org/10.2475/05.2007.01

Meyers, S. R., Sageman, B. B., & Hinnov, L. A. (2001). Integrated quantitative stratigraphy of the Cenomanian-Turonian Bridge Creek Limestone Member using evolutive harmonic analysis and stratigraphic modeling. *Journal of Sedimentary Research*, *71*(4), 628–644. https://doi.org/10.1306/012401710628

Mitchell, W. I. (2004). Carboniferous. In *Chap.7. The geology of Northern Ireland-our natural foundation* (pp. 79–116). Geological Survey of Northern Ireland.

Montañez, I. P. (2022). Current synthesis of the penultimate icehouse and its imprint on the Upper Devonian through Permian stratigraphic record. In S. G. Lucas, J. W. Schneider, X. Wang, & S. Nikolaeva (Eds.), *The Carboniferous timescale 2022* (Vol. 512, pp. 213–245). Geological Society, London, Special Publications.

Mount, J. F. (1984). Mixing of siliciclastic and carbonate sediments in shallow shelf environments. *Geology*, *12*(7), 432–435. https://doi.org/10.1130/0091-7613(1984)12<432:mosacs>2.0.co;2

Muhs, D. R., Budahn, J. R., Prospero, J. M., Skipp, G., & Herwitz, S. R. (2012). Soil genesis on the island of Bermuda in the Quaternary: The importance of African dust transport and deposition. *Journal of Geophysical Research*, *117*(F3). https://doi.org/10.1029/2012JF002366

Opluštil, S., Laurin, J., Hýlová, L., Jirásek, J., Schmitz, M., & Sivek, M. (2022). Coal-bearing fluvial cycles of the late Paleozoic tropics; astronomical control on sediment supply constrained by high-precision radioisotopic ages, Upper Silesian Basin. *Earth-Science Reviews*, *228*, 103998. https://doi.org/10.1016/j.earscirev.2022.103998

Pazukhin, V. N., Kulagina, E. I., Nikolaeva, S. V., Kochetova, N. N., & Konovalova, V. A. (2010). The Serpukhovian stage in the Verkhnyaya Kardailovka section, South Urals. *Stratigraphy and Geological Correlation*, *18*(3), 269–289. https://doi.org/10.1134/S0869593810030044

Peters, C., & Dekkers, M. J. (2003). Selected room temperature magnetic parameters as a function of mineralogy, concentration and grain size. *Physics and Chemistry of the Earth, Parts A/B/C*, *28*(16–19), 659–667. https://doi.org/10.1016/s1474-7065(03)00120-7

Peters, C., & Thompson, R. (1998). Magnetic identification of selected natural iron oxides and sulphides. *Journal of Magnetism and Magnetic Materials*, *183*(3), 365–374. https://doi.org/10.1016/s0304-8853(97)01097-4

Pointon, M. A. (2012). *Constraining global Carboniferous climatic fluctuations using high resolution geochronology* PhD thesis. University of Dublin. (unpublished) Retrieved from http://www.tara.tcd.ie/handle/2262/78167

Pointon, M. A., Chew, D. M., Ovtcharova, M., Sevastopulo, G. D., & Delcambre, B. (2014). High-precision U–Pb zircon CA-ID-TIMS dates from western European late Viséan bentonites. *Journal of the Geological Society*, *171*(5), 649–658. https://doi.org/10.1144/jgs2013-106

Pointon, M. A., Cliff, R. A., & Chew, D. M. (2012). The provenance of Western Irish Namurian Basin sedimentary strata inferred using detrital zircon U-Pb LA-ICP-MS geochronology. *Geological Journal*, *47*(1), 77–98. https://doi.org/10.1002/gj.1335

Razik, S., Dekkers, M. J., & von Dobeneck, T. (2014). How environmental magnetism can enhance the interpretational value of grain-size analysis: A time-slice study on sediment export to the NW African margin in Heinrich Stadial 1 and mid Holocene. *Palaeogeography, Palaeoclimatology, Palaeoecology*, *406*, 33–48. https://doi.org/10.1016/j.palaeo.2014.04.009

R Core Team, R. (2013). *R: A language and environment for statistical computing*. R Foundation for Statistical Computing.

25724525, 2024, 3, Downloaded from https://agupubs.onlinelibrary.wiley.com/doi/10.1029/2023PA004772 by Spanish Cochrane National Provision (Ministerio de Sanidad), Wiley Online Library on [02/04/2024]. See the Terms and Conditions (https://onlinelibrary.wiley.com/terms-and-conditions) on Wiley Online Library for rules of use; OA articles are governed by the applicable Creative Commons License

Schaaf, M., & Thurow, J. (1997). Tracing short cycles in long records: The study of inter-annual to inter-centennial climate change from long sediment records, examples from the Santa Barbara basin. *Journal of the Geological Society*, *154*(4), 613–622. https://doi.org/10.1144/gsjgs.154.4.0613

Schmidt, V., Günther, D., & Hirt, A. M. (2006). Magnetic anisotropy of calcite at room-temperature. *Tectonophysics*, *418*(1–2), 63–73. https://doi.org/10.1016/j.tecto.2005.12.019

Schmitz, M. D., & Davydov, V. I. (2012). Quantitative radiometric and biostratigraphic calibration of the Pennsylvanian–Early Permian (Cisuralian) time scale and pan-Euramerican chronostratigraphic correlation. *GSA Bulletin*, *124*(3–4), 549–577. https://doi.org/10.1130/b30385.1

Schwarzacher, W. (1961). The stratification of the great scar limestone in the settle district of Yorkshire. *Geological Journal*, *2*(1), 124–142. https://doi.org/10.1002/gj.3350020113

Shin, J. Y., Hyeong, K., & Kim, W. (2021). A sediment magnetic record in the North Pacific across the Mid-Pleistocene transition and its implication on Asian dust evolution. *Frontiers in Earth Science*, *9*. https://doi.org/10.3389/feart.2021.789584

Sinnesael, M., McLaughlin, P. I., Desrochers, A., Mauviel, A., De Weirdt, J., Claeys, P., & Vandenbroucke, T. R. (2021). Precession-driven climate cycles and time scale prior to the Hirnantian glacial maximum. *Geology*, *49*(11), 1295–1300. https://doi.org/10.1130/g49083.1

Somerville, I. D. (1977). *The sedimentology and stratigraphy of the Dinantian limestones in the Llangollen area and east of the Clwydian Range, North Wales* PhD. Thesis (p. 234). Queen's University of Belfast. (unpublished).

Somerville, I. D. (1979a). A cyclicity in the early Brigantian (D2) limestones east of the Clwydian Range, North Wales and its use in correlation. *Geological Journal*, *14*(2), 69–86. https://doi.org/10.1002/gj.3350140205

Somerville, I. D. (1979b). Minor sedimentary cyclicity in late Asbian (upper D1) limestones in the Llangollen district of North Wales. *Proceedings of the Yorkshire Geological Society*, *42*(3), 317–341. https://doi.org/10.1144/pygs.42.3.317

Soreghan, G. S., Heavens, N. G., Pfeifer, L. S., & Soreghan, M. J. (2023). Dust and loess as archives and agents of climate and climate change in the Late Paleozoic Earth system. In S. G. Lucas, W. A. DiMichele, S. Opluštil, & K. Wang (Eds.), *Ice ages, climate dynamics and biotic events: The late Pennsylvanian World* (Vol. 535, pp. 195–233). Geological Society, London, Special Publications. https://doi.org/10.1144/SP535-2022-208

Strasser, A. (2016). Hiatuses and condensation: An estimation of time lost on a shallow carbonate platform. *The Depositional Record*, *1*(2), 91–117. https://doi.org/10.1002/dep2.9

Strasser, A. (2018). Cyclostratigraphy of shallow-marine carbonates–limitations and opportunities. In M. Montenari (Ed.), *Stratigraphy and timescales*, *Cyclostratigraphy and astrochronology* (Vol. 3, pp. 151–187). Academic Press. https://doi.org/10.1016/bs.sats.2018.07.001

Thompson, R., & Morton, D. J. (1979). Magnetic susceptibility and particle-size distribution in recent sediments of the Loch Lomond drainage basin, Scotland. *Journal of Sedimentary Research*, *49*, 801–811. https://doi.org/10.1306/212f7851-2b24-11d7-8648000102c1865d

Thran, A. C., East, M., Webster, J. M., Salles, T., & Petit, C. (2020). The influence of carbonate platforms on the geomorphological development of a mixed carbonate-siliciclastic margin (Great Barrier Reef, Australia). *Geochemistry, Geophysics, Geosystems*, *21*(4). https://doi.org/10.1029/2020GC008915

Thurlow, A. D. (1996). *Sedimentary style in a mixed carbonate-siliciclastic depositional setting: The late Dinantian of Northwest Cumbria* PhD. University of Manchester. (unpublished) Retrieved from https://www.proquest.com/openview/cbcadcabe341af80bb62518fd18e8b87/1?pq-origsite=gscholar&cbl=2026366&diss=y

Tucker, M. E., Gallagher, J., & Leng, M. J. (2009). Are beds in shelf carbonates millennial-scale cycles? An example from the mid-Carboniferous of northern England. *Sedimentary Geology*, *214*(1–4), 19–34. https://doi.org/10.1016/j.sedgeo.2008.03.011

Ueno, K., Hayakawa, N., Nakazawa, T., Wang, Y., & Wang, X. (2013). Pennsylvanian–early Permian cyclothemic succession on the Yangtze carbonate platform, South China. In A. Gąsiewicz & M. Słowakiewicz (Eds.), *Palaeozoic climate cycles: Their evolutionary and sedimentological impact* (Vol. 376, pp. 235–267). Geological Society of London, Special Publications.

Van der Zwan, C. J. (2002). The impact of Milankovitch-scale climatic forcing on sediment supply. *Sedimentary Geology*, *147*(3–4), 271–294. https://doi.org/10.1016/s0037-0738(01)00130-0

Vanstone, S. D. (1993). *Soil development and the use of palaeosols in the assessment of palaeoclimate: A case study from the late Dinantian of Britain and Newfoundland* PhD thesis. University of Reading. (unpublished).

Vanstone, S. D. (1996). The influence of climatic change on exposure surface development: A case study from the late Dinantian of England and Wales. In P. Strogen, I. D. Somerville, & G. L. L. Jones (Eds.), *Recent advances in lower Carboniferous geology* (Vol. 107, pp. 281–302). Geological Society, London, Special Publications.

Vanstone, S. D. (1998). Late Dinantian palaeokarst of England and Wales: Implications for exposure surface development. *Sedimentology*, *45*(1), 19–37. https://doi.org/10.1046/j.1365-3091.1998.00132.x

Vieira, F. V., Bastos, A. C., Quaresma, V. S., Leite, M. D., Costa, A., Jr., Oliveira, K. S., et al. (2019). Along-shelf changes in mixed carbonate-siliciclastic sedimentation patterns. *Continental Shelf Research*, *187*, 103964. https://doi.org/10.1016/j.csr.2019.103964

Wakefield, O., Waters, C. N., & Smith, N. J. P. (2016). *Carboniferous stratigraphical correlation and interpretation in the Irish Sea* (p. 82). British Geological Survey Commissioned Report, CR/16/040.

Walden, J. (1999). Remanence measurements. In J. Walden, F. Oldfield, & J. Smith (Eds.), *Environmental magnetism: A practical guide, Quaternary Research association, technical guide 6* (pp. 63–88).

Walkden, G. M. (1972). The mineralogy and origin of interbedded clay wayboards in the Lower Carboniferous of the Derbyshire Dome. *Geological Journal*, *8*(1), 143–160. https://doi.org/10.1002/gj.3350080113

Walkden, G. M. (1974). Palaeokarstic surfaces in upper Visean (Carboniferous) limestones of the Derbyshire Block, England. *Journal of Sedimentary Research*, *44*, 1232–1247. https://doi.org/10.1306/212f6c80-2b24-11d7-8648000102c1865d

Waltham, D. (2015). Milankovitch period uncertainties and their impact on cyclostratigraphy. *Journal of Sedimentary Research*, *85*(8), 990–998. https://doi.org/10.2110/jsr.2015.66

Weedon, G. P. (2022a). Problems with the current practice of spectral analysis in cyclostratigraphy: Avoiding false detection of regular cyclicity. *Earth-Science Reviews*, *235*, 104261. https://doi.org/10.1016/j.earscirev.2022.104261

Weedon, G. P. (2022b). Cyclostratigraphy: Regular cycles detected and counted to measure time. In A. L. Coe (Ed.), *Deciphering Earth's history: The practice of stratigraphy* (pp. 161–179). Geological Society of London London.

Wilson, J. L. (1967). Cyclic and reciprocal sedimentation in Virgilian strata of southern New Mexico. *Geological Society of America Bulletin*, *78*(7), 805–818. https://doi.org/10.1130/0016-7606(1967)78[805:carsiv]2.0.co;2

Winckler, G., Anderson, R. F., Fleisher, M. Q., McGee, D., & Mahowald, N. (2008). Covariant glacial-interglacial dust fluxes in the equatorial Pacific and Antarctica. *Science*, *320*(5872), 93–96. https://doi.org/10.1126/science.1150595

Wright, V. P. (1992). A revised classification of limestones. *Sedimentary Geology*, *76*(3–4), 177–185. https://doi.org/10.1016/0037-0738(92)90082-3

25724525, 2024, 3, Downloaded from https://agupubs.onlinelibrary.wiley.com/doi/10.1029/2023PA004772 by Spanish Cochrane National Provision (Ministerio de Sanidad), Wiley Online Library on [02/04/2024]. See the Terms and Conditions (https://onlinelibrary.wiley.com/terms-and-conditions) on Wiley Online Library for rules of use; OA articles are governed by the applicable Creative Commons License

Wright, V. P., Vanstone, S. D., & Marshall, J. D. (1997). Contrasting flooding histories of Mississippian carbonate platforms revealed by marine alteration effects in palaeosols. *Sedimentology*, *44*(5), 825–842. https://doi.org/10.1046/j.1365-3091.1997.d01-51.x

Zhang, Q., Liu, Q., & Sun, Y. (2020). Review of recent developments in aeolian dust signals of sediments from the North Pacific Ocean based on magnetic minerals. *Geological Magazine*, *157*(5), 790–805. https://doi.org/10.1017/s0016756819000712

Zheng, H., Oldfield, F., Yu, L., Shaw, J., & An, Z. (1991). The magnetic properties of particle-sized samples from the Luo Chuan loess section: Evidence for pedogenesis. *Physics of the Earth and Planetary Interiors*, *68*(3–4), 250–258. https://doi.org/10.1016/0031-9201(91)90044-i

Zhou, M., Wu, H., Hinnov, L. A., Fang, Q., Zhang, S., Yang, T., & Shi, M. (2022). Empirical reconstruction of Earth-Moon and solar system dynamical parameters for the past 2.5 billion years from cyclostratigraphy. *Geophysical Research Letters*, *49*(16). https://doi.org/10.1029/2022GL098304

Zou, Z., Huang, C., Li, M., & Zhang, Y. (2016). Climate change response to astronomical forcing during the Oligocene-Miocene transition in the equatorial Atlantic (ODP Site 926). *Science China Earth Sciences*, *59*(8), 1665–1673. https://doi.org/10.1007/s11430-016-5311-y

References From the Supporting Information

Berger, A., Loutre, M. F., & Laskar, J. (1992). Stability of the astronomical frequencies over the Earth's history for paleoclimate studies. *Science*, *255*(5044), 560–566. https://doi.org/10.1126/science.255.5044.560

Booth, C. A., Walden, J., Neal, A., Smith, J. P., & Morgan, E. (2004). A comparison of inter-site, intra-site, inter-sample and instrument variability in environmental magnetic data: An example based on the Gwendraeth Estuary, south Wales, UK. *Journal of Coastal Research*, *20*, 808–813. https://doi.org/10.2112/1551-5036(2004)20[808:acoiii]2.0.co;2

Chatfield, C. (2004). *The analysis of time series: An introduction* (6th ed.). CRC Press.

Hounslow, M. W., Horng, C. S., & Karloukovski, V. (2023b). Rotational remanent magnetization as a magnetic mineral diagnostic tool at low rotation rates. *Geophysical Journal International*, *232*(1), 300–321. https://doi.org/10.1093/gji/ggac330

Strank, A. R. E. (1981). *Foraminiferal biostratigraphy of the Holkerian, Asbian and Brigantian stages of the British lower Carboniferous* Ph.D. Thesis. University of Manchester. (unpublished).

Vaughan, S., Bailey, R. J., & Smith, D. G. (2015). Cyclostratigraphy: Data filtering as a source of spurious spectral peaks. In D. G. Smith, R. J. Bailey, P. M. Burgess, & A. J. Fraser (Eds.), *Strata and time: Probing the Gaps in our understanding* (Vol. 404, pp. 151–156). Geological Society, London, Special Publications.

Weedon, G. P. (2003). *Time-series analysis and cyclostratigraphy: Examining stratigraphic records of environmental cycles*. Cambridge University Press.

25724525, 2024, 3, Downloaded from https://agupubs.onlinelibrary.wiley.com/doi/10.1029/2023PA004772 by Spanish Cochrane National Provision (Ministerio de Sanidad), Wiley Online Library on [02/04/2024]. See the Terms and Conditions (https://onlinelibrary.wiley.com/terms-and-conditions) on Wiley Online Library for rules of use; OA articles are governed by the applicable Creative Commons License